Article

by Abiola Oyebamiji[1,2,3], Ruizhong Hu[1,2]*, Chenghai Zhao[1], Aizat Zhaanbaeva[1], and Tehseen Zafar[1]

Ore genesis of the Qilinchang Carboniferous carbonate Pb-Zn Mississippi Valley-type deposit, Western Yangtze Platform, Southwest China: Constraints from mineralogy, C-O-S-Pb isotope systematics, and REE studies

[1] State Key Laboratory of Ore Deposit Geochemistry, Institute of Geochemistry, Chinese Academy of Sciences, Guiyang 550081, China;
*Corresponding author, *E-mail: huruizhong@vip.gyig.ac.cn*
[2] College of Earth and Planetary Sciences, University of Chinese Academy of Sciences, Beijing 100049, China
[3] Department of Science Laboratory Technology, (Geology unit) Ekiti State University, Ado-Ekiti, Nigeria

(Received: June 23, 2019; Revised accepted: January 25, 2020)

https://doi.org/10.18814/epiiugs/2020/020050

The (Pb-Zn)-Ag-Ge deposits of the Qilinchang deposit (Western Yangtze Platform, southwest China) are hosted by a 20 m thick sequence of Early Carboniferous carbonate rocks of the Baizuo Formation. Sulfide mineralization consists mainly of pyrite sphalerite, galena, chalcopyrite, and marmatite, while gangue minerals are dolomite, calcite, and quartz. Bulk carbon and oxygen isotope analysis were determined on syngenetic calcite associated with mineralization. The $\delta^{13}C_{PDB}$ and $\delta^{18}O_{SMOW}$ values range from –2.35 to –0.37‰ and +19.24 to +26.83‰, respectively. These values reveal that the ore-forming fluids were predominantly derived from water/rock interaction between the mantle/metamorphic fluids and carbonates. Sulfur isotope compositions range from +12.33 to +17.01‰ are consistent with thermochemical reduction (TSR) of Carboniferous seawater sulfate. Sulfur is mainly derived from evaporite rocks hosted in the strata, relatively producing H_2S–rich fluids evaporated by TSR. The homogenous lead isotope ratios for galena and sphalerite suggest that Pb was sourced from the basement rocks of Kunyang Group and Cambrian to Permian strata. The total REE (∑REE) compositions for calcite, pyrite, galena, and sphalerite indicate that the input of REE in the fluids was probably obtained from carbonate host rocks. All combined data propose multiple or mixed sources.

Introduction

Carbonate-hosted, low-temperature, strata-bound, Pb-Zn deposits, are significant group of sediment-hosted Pb-Zn deposits (Leach et al., 2005, 2010), and are generally referred to as Mississippi Valley-type (MVT) deposits coined after the occurrence of many such deposits within the drainage basin of the Mississippi River in the central United States (Brannon et al., 1992; Heijlen et al., 2003; Muchez et al., 2005). Deposits of this nature are globally distributed and are located in regions such as the mid-continent region of North America, Southeast Asia, North Africa, and Western Europe. The base metal deposits in the Sichuan-Yunnan-Guizhou (SYG) metallogenic province contain over and above 400 known Pb-Zn deposits with total Pb+Zn metal reserves of approximately 26 million tons (Liu and Lin, 1999; Huang et al., 2003; Han et al., 2007; Zaw et al., 2007; Zhou et al., 2013a, b, c, d, e; Zhang et al., 2015). Tectonically, this SYG minerogenetic domain is westbound on the Yangtze Platform, southwestern part of China.

Previous studies on the world-class Huize carbonate-hosted Pb-Zn deposits (Han et al., 2007) have classified these deposits to be super-large in scale, consistent and highly extractable ore quality, germanium-, lead-, and zinc-rich. These studies are predicated on the geological background of the deposit areas (Xie, 1963; Tu, 1984; Zhang, 1984), the isotope and element geochemistry (Huang et al., 2003; Han et al., 2004, 2007, 2012; Li et al., 2004, 2006; Zhang et al., 2006), the tectonic and geological setting of the ore fields (Han et al., 2001, 2006, 2014), and the provenance of the mineralizing fluids responsible for the formation of the deposits (Huang et al., 2003; Han et al., 2001, 2006; Zhang 2008). In all these studies, they have only proved that these deposits in the SYG province have a couple of identical characteristics, amongst (i) hosted by siliceous dolostones of Sinian (Mesoproterozoic to early Neoproterozoic) to Permian (upper Palaeozoic), (ii) ores are located and controlled in thrust faults and/or fold structures, (iii) consistent high-grade of total Pb + Zn (25–35%, with some exceeding 60%), (iv) temporally and three-dimensionally linked to the Emeishan basalts of the upper Permian (ca. ~260 Ma), Sm–Nd isotopic studies of calcite, indicating isochron ages of 226 ± 15 Ma and 225 ± 38 Ma for the Qilinchang and Kuangshanchang ore, greatly younger compared to the flood basalts (Hu and Zhou, 2012; 2013a, b, c, d, e, 2014; Zhang et al.,

2015) and (v) the ore-forming fluids of these deposits are characteristic of moderate temperatures of 150–280 °C and low to moderate salinity of 4–15 wt.% NaCl (Zhang et al., 2005a; Han et al., 2007).

Based on the evidence of past works, there have been contradicting opinions and conclusions on the formation of these super-large Pb-Zn deposits. Such arguments include Zhang, 1984; Shen, 1988; Zhang and Yuan, 1988; Zhang, 1989; Chen, 1993; Zhao, 1995; conjectured that the Emeishan basalt magmatic-hydrothermal mobilization and enrichment which eventuated during the Indosinian-Yanshanian tectonic localization associated with sedimentary-reworking are responsible factors for the deposition of the ores. Consequently, Liu and Lin (1999), postulated that the metallogenic fluids are mainly extracted by deeply-circulating geothermal water-filling through the subsurface layers. Contrastingly, Han et al. (2004, 2007), believed that the source of sulfur in the mineralizing fluids originates mainly from carbonate strata, while the fluid is preponderantly extracted from the Kunyang Group basement rocks and the evaporite-bearing rocks of the cover strata. Li et al. (2005), hypothesized that the basinal fluids were likely derived by thermochemical sulfate reduction of sulfates within the strata. Also, Huang et al. (2003), suggested using carbon and oxygen isotope of calcite and ore–hosting strata, theorized that the ore-forming fluids represent crustal-mantle fluid mixing. Latterly, Zhang et al. (2017), identified dual types of metallogenic fluid using C-H-O isotopic measurements of carbonates and proposed that the ore-forming fluids are formed because of capacious fluid migration from deep regions of the crust. In all of these, the origins of the metallogenic fluids of the Huize deposit remain controversial despite the large volume of detailed studies that have been carried out in this region.

The application of isotopes of C-O-S-Pb is an efficient tool for determining sources of chemical compositions in ore-forming fluids (Ohmoto and Goldhaber, 1997; Li et al., 2007; Rddad et al., 2018; Zhou et al., 2018). Hence, we make use of the Qilinchang deposit as a case study by analyzing the REE composition of calcite and sulfide, carbon, and oxygen isotopes of syngenetic-ore calcite, sulfur, and lead isotopes of the sulfide together with an emphatic description of the geology and mineralogy. With these new datasets, we discuss the genesis of the ore-forming fluids and propound a model that will further constraint the formation of Pb-Zn sulfide minerals in the geochemical province.

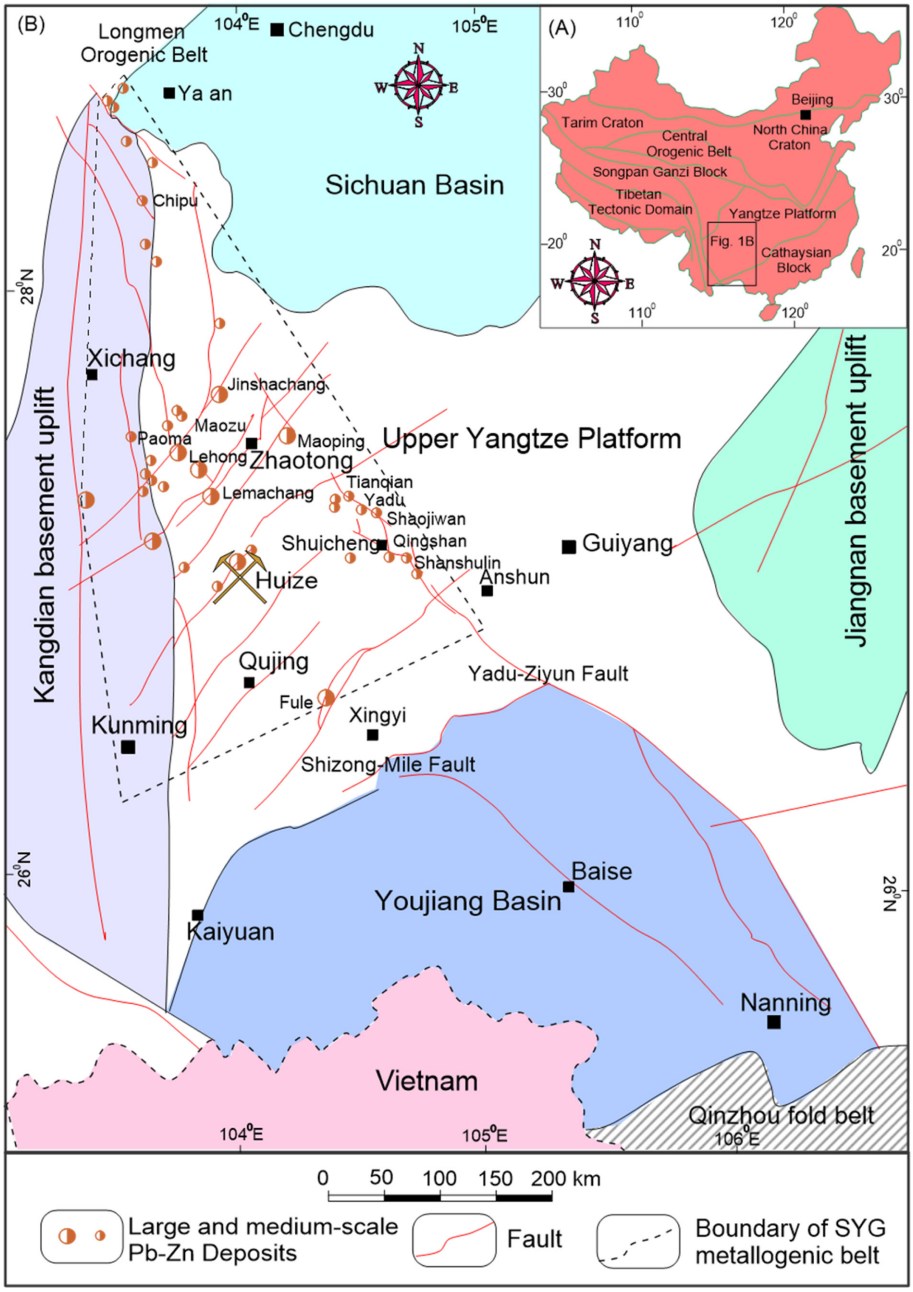

Figure 1. (A) Tectonic map of South China. (B) Major sediment-hosted Pb–Zn deposits in the Sichuan–Yunnan–Guizhou (SYG) triangular metallogenic province (Modified after Liu and Lin, 1999).

Geological Setting

Regional Geology

In southwest China, the SYG metallogenic province is located adjacent to the southwestern margin of the Yangtze Platform (Fig. 1A). The Yangtze Platform is bounded to the west by the Tibetan Tectonic Domain (TTD), to the east by the Cathaysian Block (CB) and to the south by the Indochina Block (IB). The Yangtze Platform (Fig. 1B) is made up of Archean to the Proterozoic rocks and Palaeozoic-Mesozoic sedimentary strata (Zhou et al., 2002b; Yan et al., 2003). The folded basement rocks in this region comprise those of the Kangding, Dahongshan, and Kunyang Groups (Mesoproterozoic–Early Neoproterozoic). It is composed of tightly packed sandstones, slates, greywackes, shale, dolostone, and carbonaceous to a siliceous sedimentary sequence that is closely folded but weakly metamorphosed (Sun et al., 2009). The Mesoproterozoic to the early Neoproterozoic rocks of the Kunyang Group is believed to have been formed in a foreland basinal setting

(Li et al., 2013; Jin et al., 2016). The overlying sedimentary cover which lies unconformably above the Kunyang Group is composed of Palaeozoic to lower Mesozoic strata of shallow marine origin (Yan et al., 2003), and clastic sedimentary stratigraphic units in a rifted continental slope and the late Triassic to Cenozoic strata of continental facies (Liu and Lin, 1999). The Sinian Dengying Formation consists of pale siliceous dolostone, dark argillaceous shale interbedded with yellowish sandy mudstone of the Dengying Formation. The Dengying Formation dolostone is about 1 km thick and is believed to host plausible prospecting potential at the depth and/or out of the Huize orefield.

A wide deposit of sublittoral to neritic facies of lower Palaeozoic to Carboniferous sedimentary rocks composed of gray aphanitic limestone, medium-grained dolostone, and sandstone, are overlain by gray to dark brown, mainly massive with localized amygdaloidal and vesicular structures of the Emeishan large igneous province in the late Middle Permian with a peak age of 259±1 Ma (Zhou et al., 2002b; Ali et al., 2005; Zhong et al., 2014). The Emeishan flood basalt has discordant contact with underlain strata, and it covers an area of about 500,000 km^2 (Zhou et al., 2002b).

The lower Carboniferous Baizuo Formation is about 40–60 m in thickness and consists of grey, yellowish, and pink coarse-grained dolostone with dolomitic limestone and light grey limestone interbed. The lower Carboniferous Datang Formation has a thickness of 5–25 m and primarily consists of grey aphanitic limestone and oolithic limestone, with 0.5 m thick of brownish siltstone and purplish mudstone at the upper section. The upper Devonian Zaige Formation with a thickness of 200–310 m, mainly consists of light grey to yellowish medium-grained dolostone, and argillaceous dolostone interbeds in the middle to lower part (Zhong et al., 2013). Host strata of the Pb-Zn deposits consist mainly of carbonate rocks (dolomite, dolomitic limestone, and bioclastic limestone) of the Dengying and Baizuo Formations which account for approximately 80% of the proven Pb + Zn reserves in the SYG domain (Chen et al., 2015).

Geological Features of the Huize Deposit

The Huize Pb-Zn deposit is located on either side of the near NE-, NS- and NW- trending between Qujing-Zhaotong and Xiaojiang concealed faults at the NE end of the Jinniuchang-Kuangshanchang tectonic structural belt. It consists of three structurally controlled Pb-Zn deposits, the Kuangshanchang, Qilinchang, and the medium-sized Yichangpo Pb-Zn deposits (Fig. 2), which are separated by triad NE-striking thrust faults; the Kuangshanchang, Qilinchang, and Dongtou faults. Mining operations in this district date back to the Han Dynasty, and more recently, geological exploration and exploitation begin in the 1950s.

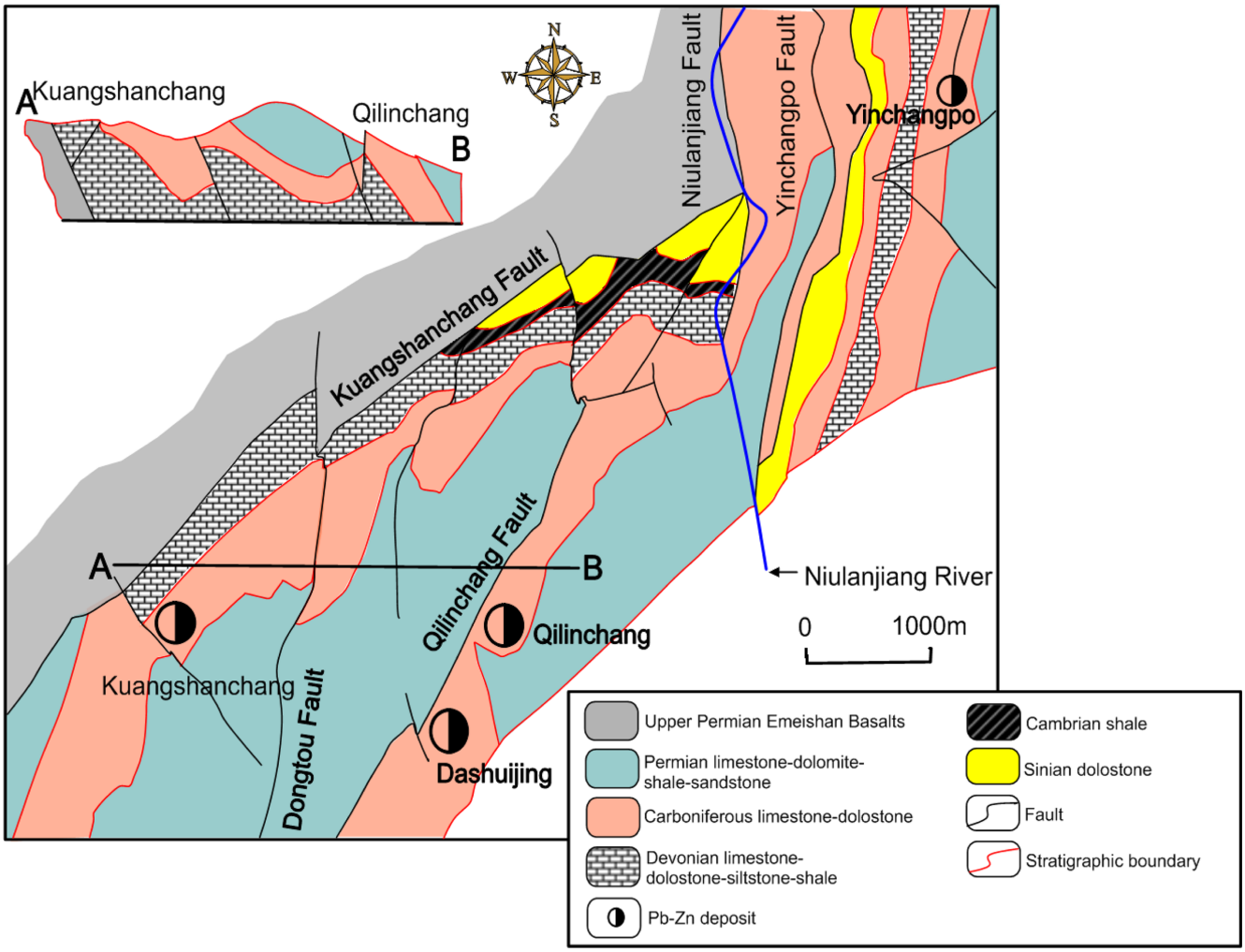

Figure 2. Simplified geological map of the Huize deposit (Modified after Han et al., 2016).

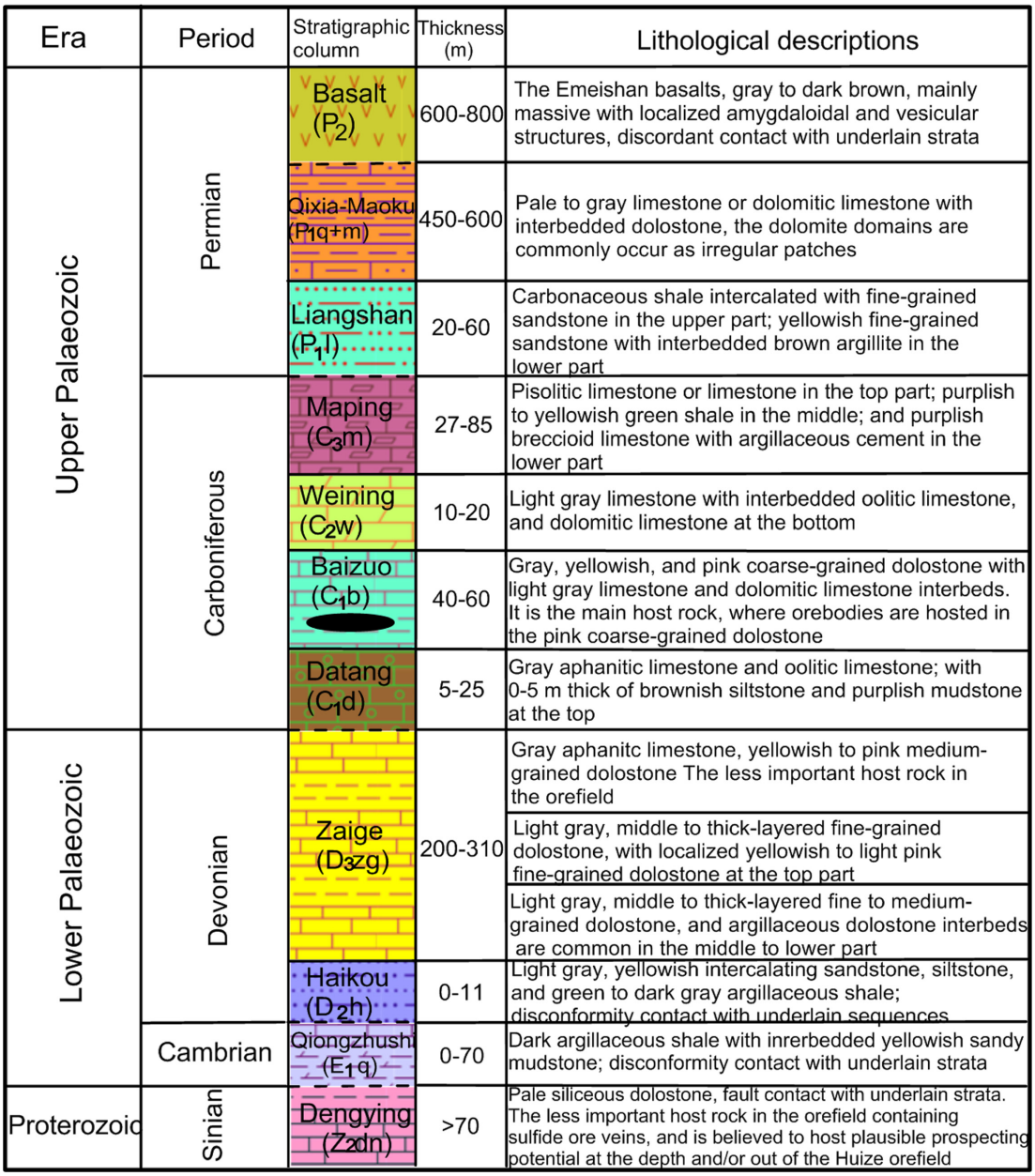

Figure 3. Schematic lithostratigraphic column for the Huize orefield showing the major facies and thickness of the sequences (Modified after Li et al., 2006).

More than 400 known Pb-Zn deposits with tally Pb+Zn reserves ranging from ten to million tonnes have been documented in the deposit. The obvious occurrence of the ore bodies is mainly hosted in the dolostones of the lower Carboniferous Baizuo Formation (Fig. 3), and plausible prospecting potential in the upper Devonian Zaige Formation (Zhou et al., 2001; Zhong et al., 2013). Based on field observations, the orebodies are primarily encased in coarse-grained dolostone with light grey limestone and dolomitic limestone interbeds of the Baizuo Formation. Alteration processes within this deposit include dolomitization, calcification, silicification, and argillization. The alteration of the host rocks is highly visible with apparent and well-defined contact between the host rocks and ore bodies, and often exhibit open-space filling characteristics of typical MVT deposits (Leach et al., 2005, 2010).

Deposit Geology

Stratigraphy and Lithology

The Qilinchang Pb-Zn deposit is positioned above the Qilinchang fault, and it is made up of Qilinchang and Dashuijing mining sections. The deposit is hosted mainly by the upper part of the lower Carboniferous Baizuo Formation dolostone (Fig. 3). The Baizuo Formation host rock massive dolostone was formed due to extensive regional dolomitization, which happened before the formation of the Qilinchang deposit. Overlying Carboniferous rocks are carbonaceous shale intercalated with fine-grained sandstone of the Liangshan Formation in the upper part and yellowish fine-grained sandstone interbedded with brown argillite in the lower section.

Structure

Fold and fault structures in the Qilinchang Pb-Zn deposit are broadened, overarching the NE-trending Qilinchang and the Dongtou fault. The Qilinchang-Dongtou thrust fault (F_1) trends N20°-30°E and steeply dipping S50-76°E. This regional structure controls the formation and localization of Pb-Zn deposits in the area. Along the horizontal plane, the ore bodies occur as flat, lensoid, vein-like, stockwork pattern; while in the vertical plane, they are mainly present in the form of lenticels with strained or pinched branches at both ends. The structural features responsible for the ore deposition depict a regional stress field comprising the anticline, syncline, principal pressure stress, compressive and tensile shear stress structural plane (σ1), all tilting to the NW-SE to generate a lateral plunge of ore bodies (Fig. 4).

Orebody Characteristics

Ore bodies in the Qilinchang deposit are controlled by massive, veined, banded, disseminated, and brecciated structures. There are four ore bodies documented in the Qilinchang deposit area, namely; No. 3, No. 6, No. 8, and No. 10 (Figs. 5 and 6), of which No. 8 is the largest. The mineral composition of the sulfide ores is comparatively simple and contains an abundant amount of sphalerite, galena, pyrite with the minor occurrence of arsenopyrite, chalcopyrite, bornite, marcasite, and native antimony. Ore bodies include over 1.9 million tons Pb-Zn ores at a grade of 2.3–9.2% Pb and 2.7–22.5% Zn, with high Zn/Pb ratios on the order of 5–14. The ores mainly incorporate major elements of Fe and S, with the occurrence of trace elements such as Ga, Ge, Cd, and Ag (Zhou et al., 2001; Han et al., 2007; Li et al., 2007 and Yin et al., 2009).

Mineral Paragenesis

Based on the hypothesis of previous works (Han et al., 2006, 2007), cross-cutting and replacement relationships, ore structures, textures, and mineral assemblage characteristics of the Qilinchang deposit, the metallogenesis can be subdivided into two periods: hydrothermal and supergene oxidizing stage. The hydrothermal period is further classified into four stages; coarse-grained pyrite-sphalerite stage, dark brown sphalerite–galena stage, galena–light yellow sphalerite stage, and fine-grained pyrite–carbonate stage (Fig. 7).

Structure and Texture of Ores

In reference to field observations and petrographic studies, the ore structures of the Qilinchang Pb-Zn deposit include massive, disseminated, veined, brecciated, miarolitic, and stockwork structures (Fig. 8a-f). These ores were subjected to hydrothermal and supergene oxi-

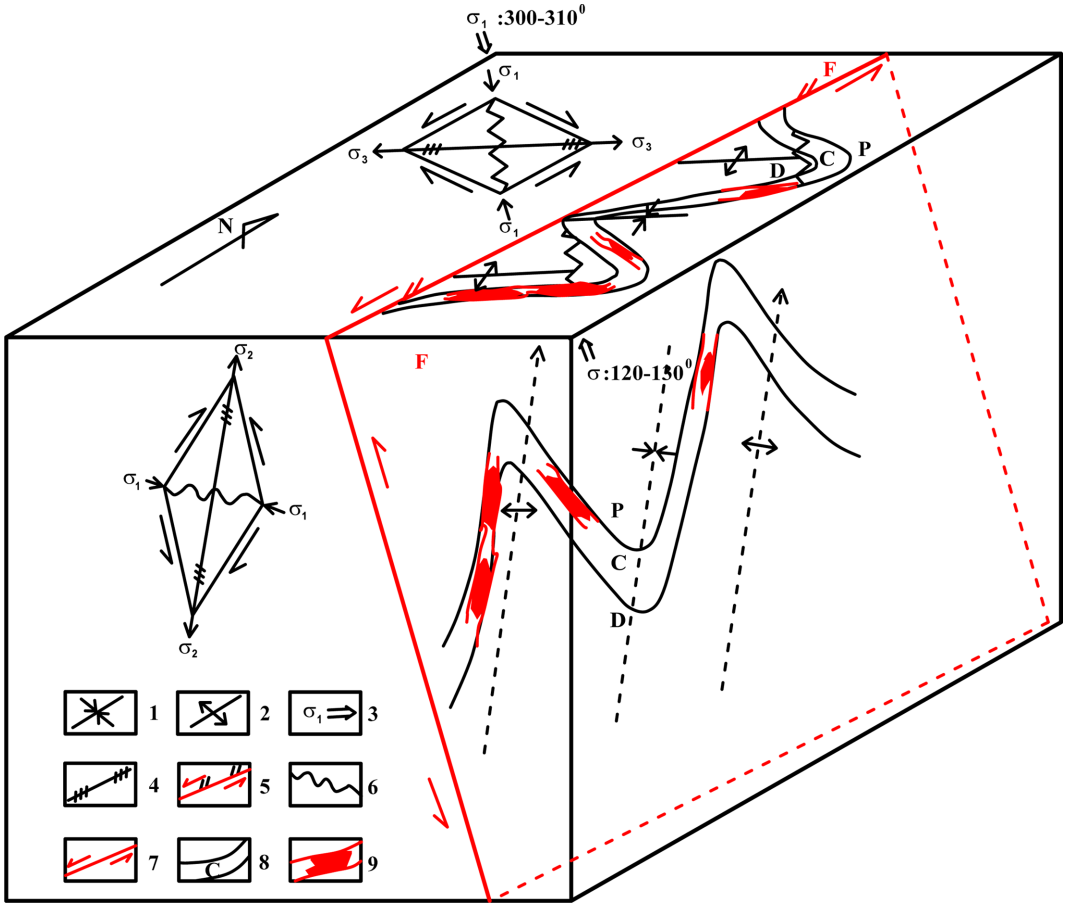

Figure 4. Box diagram of ore–controlling structures showing a regional stress field in the Huize district. 1–Syncline, 2–Anticline, 3–Principal pressure stress, 4–Compressive structure plane, 5–Compresso–shear structural plane, 6–Tensile–(shear) structural plane, 7–Moving direction of the fault, 8–Ore–hosted strata, 9–Orebody and interlayer fracture.

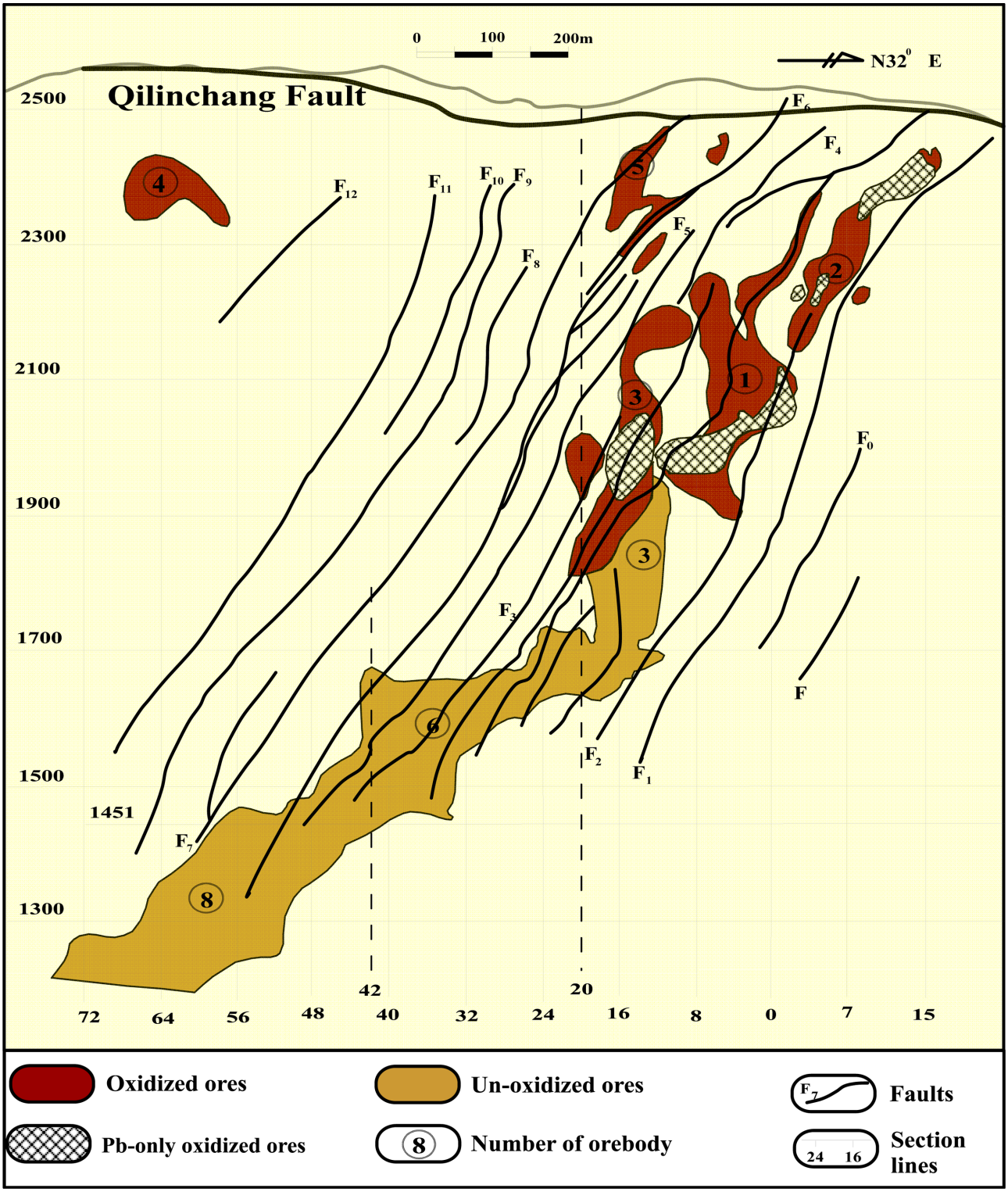

Figure 5. The vertical projection of the Qilinchang Pb–Zn–(Ag–Ge) deposit in the Huize district.

dizing processes (Han et al., 2006). There is an occurrence of oxidized and unoxidized ores along with Pb-only oxidized ores; the unoxidized ores occur at depth. There are also occurrences of mixed sulfide-oxide-ores in the transition zone. The oxidized and mixed ores have extremely complex mineral assemblages while the primary ores compositions are rather simple. The primary ore textures comprise euhedral-anhedral-grained, spongy, metasomatic, elongated, edge-shaped, void-filling, slaty cleavage, exsolution, graphic textures. Pyrite is present as a subhedral to euhedral coarse-grained crystals that occur in solid solution (Figs. 9a, b, c, and 10b, c, i, j, k). (Figs. 9d, e, f, h) show a massive, disseminated crystal of pyrite that is highly fractured, shows cataclastic texture and stress deformation. Galena is subhedral to anhedral, fine-grained, forms replacement minerals (Figs. 9d, e, f, g, i, and 10b, d, f, g, h, j, k), also show millimeter-scale fragments of a crystal (Fig.

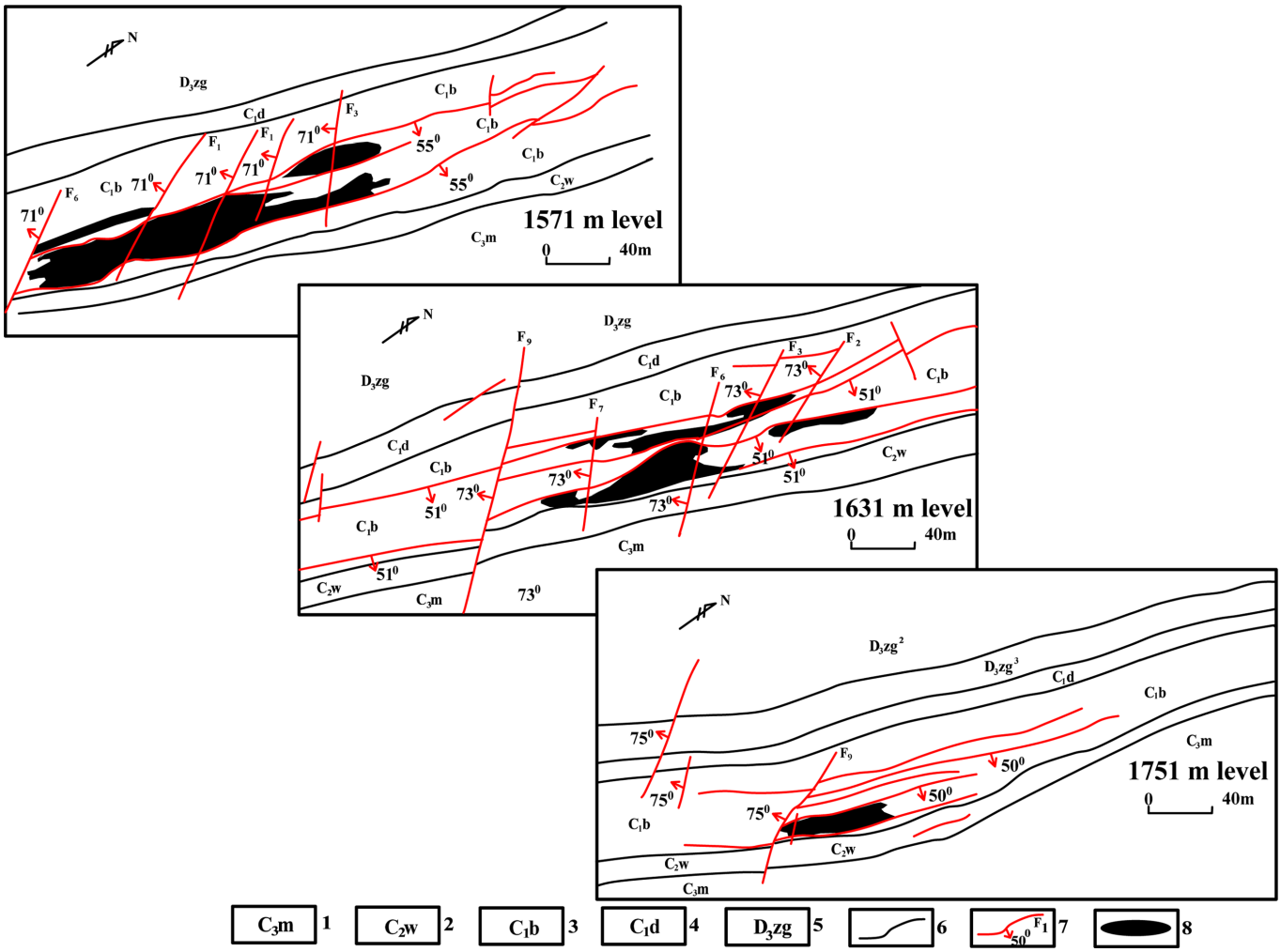

Figure 6. Planar map of No. 6 orebody in the Qilinchang Pb–Zn–(Ag–Ge) deposit, Huize. 1–Upper Carboniferous Maping formation brecciated limestone, 2–Middle Carboniferous Weining Formation limestone is intercalated with oolitic limestone, 3–Lower Carboniferous Baizuo Formation coarse crystalline dolomite intercalated with limestone and dolomitic limestone, 4–Lower Carboniferous Datang Formation cryptocrystalline limestone and oolitic limestone, 5–Upper Devonian Zaige Formation medium-coarse crystalline dolomite, 6–Stratigraphic boundaries, 7–Fault, 8–Orebody.

10a) associated with veins of calcite. Galena also occurs as a subhedral fine-grained crystal enclosed within pyrite (Fig. 10k), both surrounded by dolomite in solid solution. Sphalerite-I is present as euhedral-subhedral fine-grained crystals coexisting with galena-I (Fig. 10a) and form embayment texture with dolomite-II (Fig. 10e). Marcasite occurs as a bladed structure confined within a groundmass of sphalerite-II associated with coarse-grained galena-II (Fig. 10h). Calcite also shows centimeter-scale vein intruding massive, less fractured crystal of sphalerite-I. Edge-shaped dolomite-II is present and enclosed by galena-II (Fig. 10d, f).

Sampling and Analytical Methods

Sampling

Sphalerite, galena, and pyrite and unaltered calcite associated with the ores were obtained at the stope 8# of tunnel 1237 m in the Qilinchang underground working. These representative samples were handpicked, and individual target mineral was separated using a binocular microscope and analyzed for C, O, S, Pb isotopes, and REE.

Carbon and Oxygen Isotope Analysis

Pure, unaltered calcite separates were prepared for C and O isotope analysis at the State Key Laboratory of Ore Deposit Geochemistry, Chinese Academy of Sciences, by using a Finnigan MAT-253 mass spectrometer. The carbonate samples react with 100% phosphoric acid (H_3PO_4) to evolve CO_2 following the standard procedure of Friedman and O'Neil (1977). The reproducibility of the analytical instrument is ± 0.05 per mil ($2\sigma_m$) for $\delta^{13}C$ and ± 0.13 per mil for $\delta^{18}O$ values. Carbon and oxygen isotopic compositions are expressed relative to Vienna Pee Dee Belemnite (V-PDB) and Standard Mean Ocean Water (SMOW), respectively. $\delta^{18}O_{SMOW} = 1.03091 \times \delta^{18}O_{PDB} + 30.91$ (Coplen et al., 1983).

Sulfur Isotope Analysis

The sulfide separates (FeS_2, ZnS, and PbS) were crushed using the

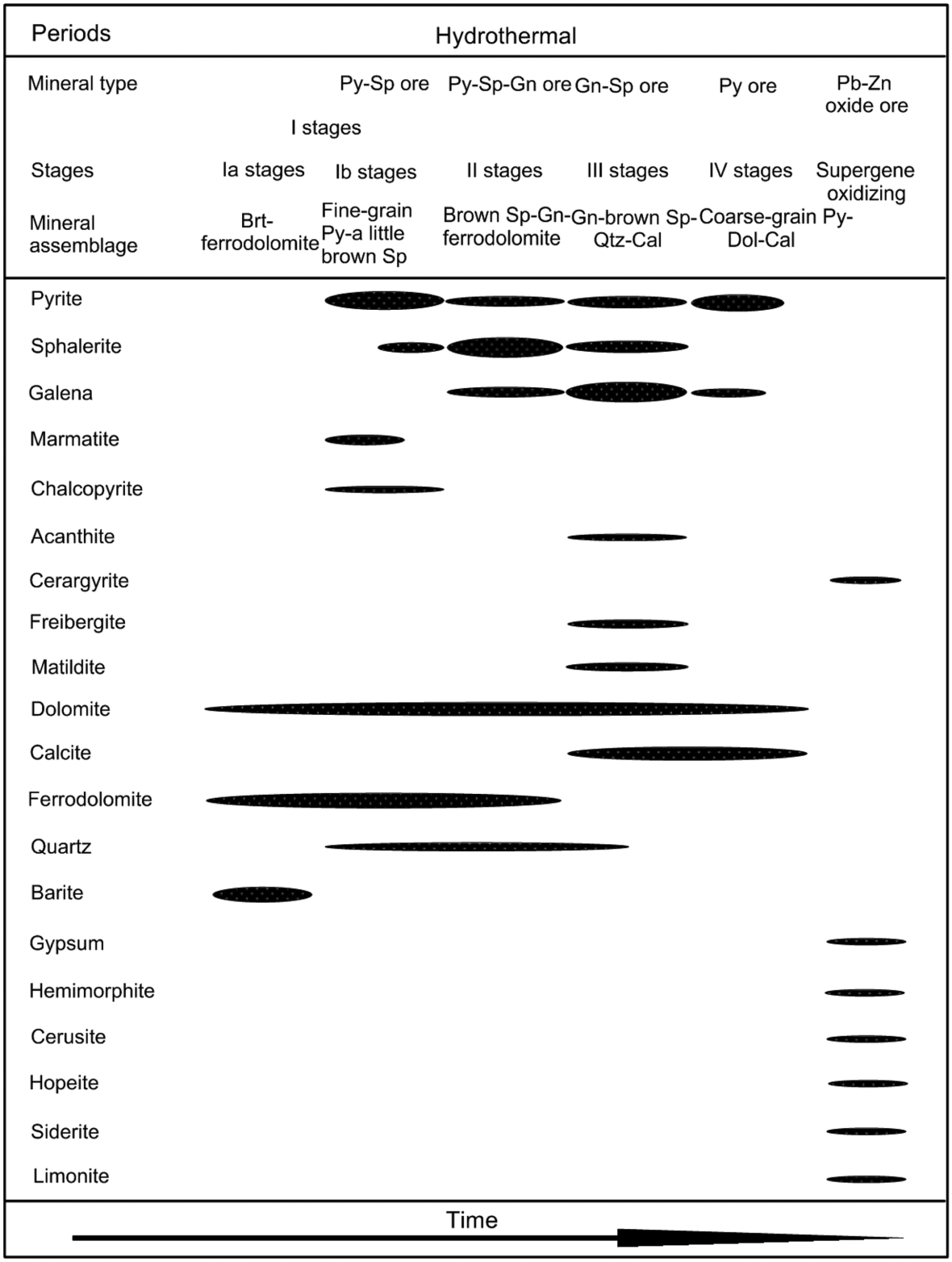

Figure 7. Paragenetic sequence in the Qilinchang Pb–Zn deposit (data are referenced from Zhang et al., 2017).

200-mesh sieve. The sulfur isotope ($\delta^{34}S$) analysis was carried out at the State Key Laboratory of Ore Deposit Geochemistry, Chinese Academy of Sciences, by using the MAT-253 continuous flow isotope mass spectrometer coupled with the Element Analyzer (EA-IRMS). The detailed analytical method described by Gao et al. (2013) was employed in this analysis. A measured weight of 112–448 μg of sulfide powders (200-mesh) was weighed and wrapped in tin capsules; the capsules were crimped and rolled into compact spheres. The analytical results are expressed relative to the Vienna Canyon Diablo Troilite (V-CDT) standard. The analytical reproducibility was better than 0.2 per mil

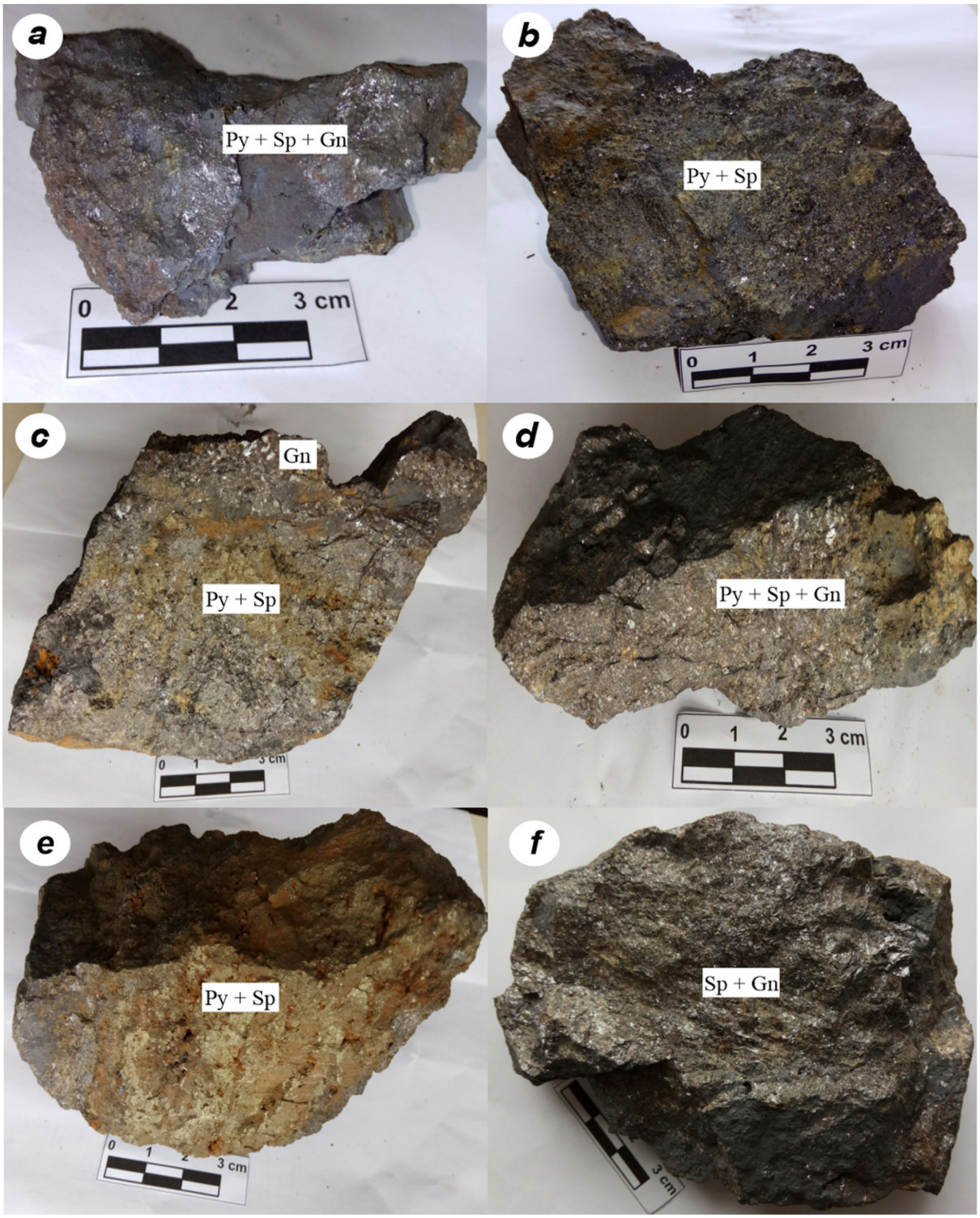

Figure 8. Photographs of hand specimens from the Qilinchang deposit; (a) massive sulfide ore, galena (Gn), sphalerite (Sp) and pyrite (Py); (b) disseminated pyrite (Py) associated with dense sphalerite (Sp); (c) vein filled with massive sphalerite (Sp) and pyrite (Py) associated galena (Gn) filling fractures; (d) brecciated pyrite (Py) associated with dense sphalerite (Sp) and galena (Gn); (e) massive vein filled with pyrite (Py) associated with sphalerite (Sp); (f) massive sphalerite (Sp) associated with fracture-filled galena (Gn).

($1\sigma_m$) as calculated using replicate analysis of the STD-S-1 (–0.25‰), STD-S-2 (+22.59‰) and STD-S-3 (–32.51‰). The precision calculated from the replicate analysis of unknown samples was also better than 0.2‰ (1σ).

Lead Isotope Analysis

The sulfide separates (PbS and ZnS) were crushed into fine particles, about 0.1 grams of the crushed samples were loaded in acid-leached

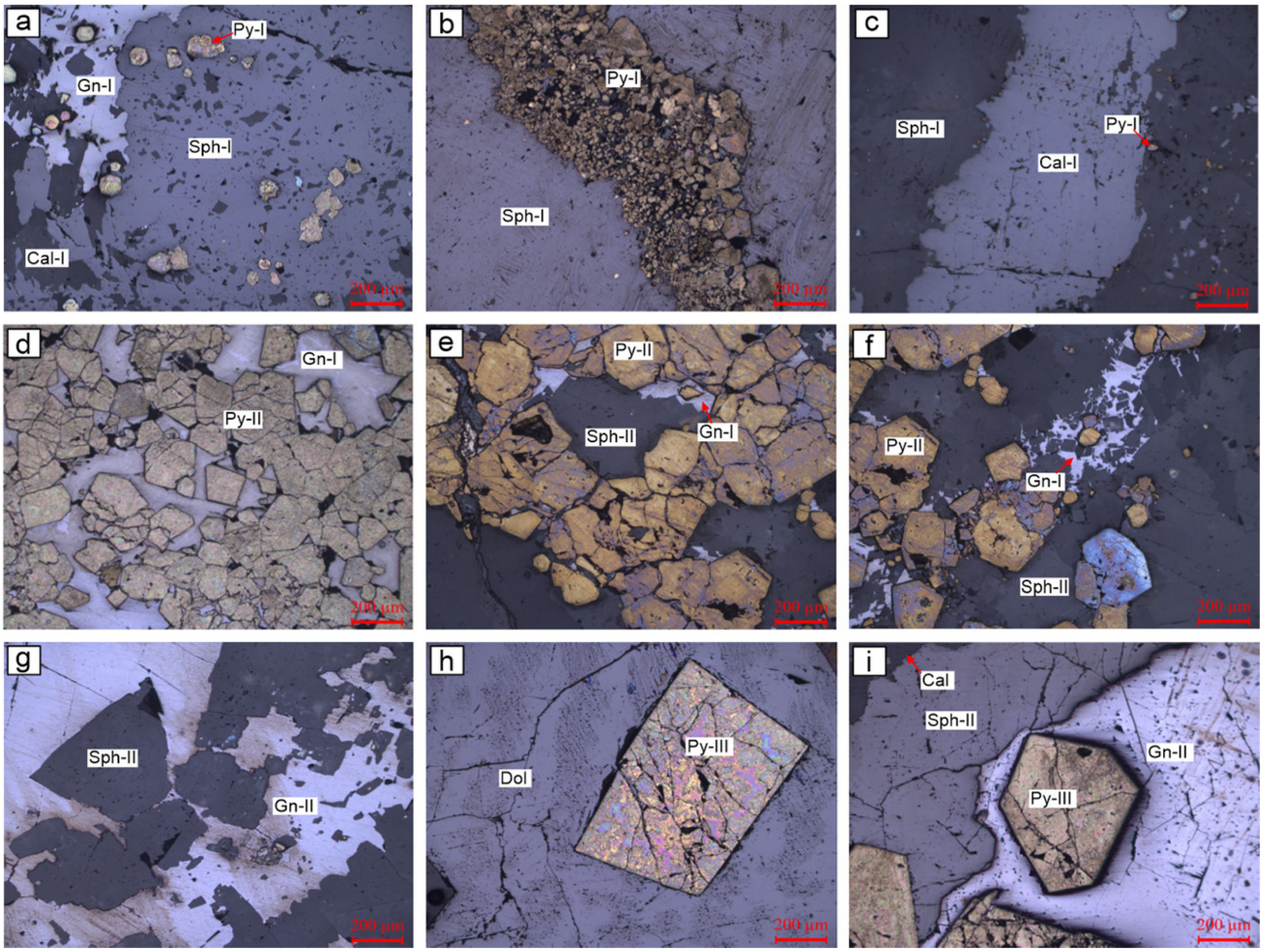

Figure 9. The textural and structural characteristics of sulfides and associated gangue minerals in the Qilinchang deposit viewed under the microscope; (a) pyrite (Py–I) occurs as subhedral–euhedral fine-grained crystals associated with galena (Gn–I), sphalerite (Sph–I), and calcite; (b) clusters of fine-grained Py–I having a cross-cutting relationship with Sph–I; (c) calcite vein cutting across Sph–I, co-existing with isolated fine-grained Py–I; (d) massive, disseminated Py–II displacing Gn–I; (e, f) massive, anhedral–subhedral, disseminated Py–II associated with Sph–II and Gn–I; (g) irregular shaped Sph–II exhibiting replacement pattern by Gn–II; (h) euhedral crystal of Py–III associated with groundmass of dolomite in a solid solution; (i) pyritohedral structure of Py–III coexisting with Gn–II, Sph–II, and calcite.

Teflon beakers. The sulfide minerals were treated chemically at the Radiogenic Isotope Ultra-Clean Laboratory at the University of Science Technology of China. The Teflon containers used for dissolution of the separated samples were immersed in cold aqua regia for about 48 hours and later placed in boiling solution of HCl and HNO_3 at an equal ratio of 1:1 for no less than 30 minutes. The detailed chemical separation of Pb followed the procedure described by Cheng and Cheng (2014). Lead isotope analyses were measured by using a Neptune Plus MC-ICP Mass Spectrometer at the State Key Laboratory of Ore Deposit Geochemistry, Chinese Academy of Sciences. The analytical procedure involved the addition of about 2 ml of 1N HNO_3 to each sample vial, the aerosol from the nebulizer is injected into the mid-region of the plasma and ionized. The average standard errors on the analyzed samples are $^{206}Pb/^{204}Pb \pm 0.001$ (2σ), $^{207}Pb/^{204}Pb \pm 0.001$ (2σ), $^{208}Pb/^{204}Pb \pm 0.002$ (2σ). Measured isotopic ratios were corrected for instrumental fractionation and agreed with reference values of the National Bureau of Standards common Pb standard NBS-981.

REE Analysis

The syngenetic calcite and primary sulfide were dissolved and analyzed for REE using the ELAN DRC-e Q-ICP-MS, at the State Key Laboratory of Ore Deposit Geochemistry, Chinese Academy of Sciences. The specific analytical technique described by Qi et al. (2000) was used for the analysis. Analytical reproducibility for REE is better than 5% (2σm).

Results

Isotopic Investigation

Carbon and Oxygen

C-O isotopic composition of syngenetic-ore calcite separates are listed in Table 1 and plotted in Fig. 11 compared with other deposits in SYG (Zhou et al., 2013d, 2014, 2018; Li et al., 2015). The $\delta^{13}C_{PDB}$ and $\delta^{18}O_{SMOW}$ values of thirteen (13) calcite extracts range from –2.35‰

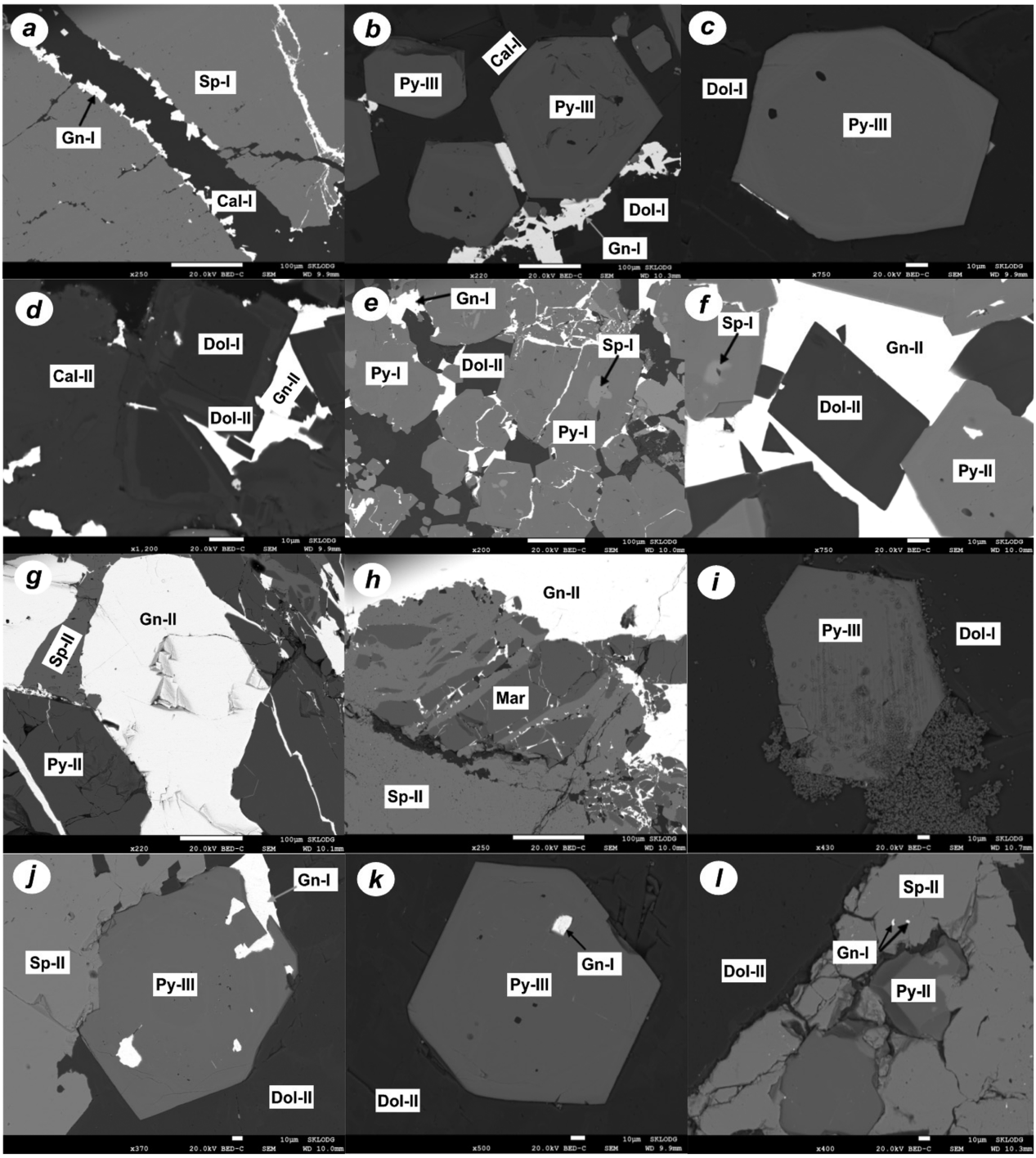

Figure 10. SEM–BSE images of polished sections illustrating the texture and structure of hydrothermal minerals in the Qilinchang deposit; (a) sphalerite–I (Sp–I) present as euhedral–subhedral fine–grained crystals coexisting with galena–I (Gn–I), both of which are intruded or filled a fracture in Sp–I with calcite–I (Cal–I) forming solid–solution; (b) pyrite–III (Py–III) present as euhedral fine–grained crystals coexist with galena–I (Gn–I) at the edges of the rims of pyrite, all enclosed by dolomite–I (Dol–I) and calcite–I (Cal–I) solid–solution; (c) euhedral, fine–grained pyrite–III (Py–III), enclosed within a groundmass of dolomite–I (Dol–I); (d) galena–II (Gn–II) coexists with calcite–II and dolomite–I, dolomite–I is later enclosed with the middle stage dolomite–II; (e) sphalerite–I (Sp–I) occur as subhedral fine–grained crystals enclosed within the early stage pyrite–I, coexisting with Gn–I, all of which form embayment texture with Dol–II, Gn–I are enclosed by Dol–II and forms fine veinlets and fill fractures in the Py–II; (f) Sp–I occurs as euhedral fine–grained crystal that is enclosed by Py–II, coexist with Gn–II and clear–edge Dol–II exhibiting solid–solution texture; (g) Py–II occurs as coarse–grained crystal coexist with fine–grained Sp–II and coarse–grained Gn–II; (h) bladed marcasite (Mar) enclosed within a groundmass of Sp–II associated with coarse–grained Gn–II; (i) euhedral, fine–grained pyrite–III (Py–III) enclosed within a groundmass of dolomite–I (Dol–I), filling pores and exhibiting replacement texture at the contact with the dolomite; (j) Sp–II present as euhedral–subhedral fine–grained crystals coexisting with Py–III and Gn–I, all of which are enclosed with Dol–II; (k) Gn–I occur as subhedral fine–grained crystal enclosed within Py–III, both of which are surrounded by Dol–II solid–solution; (l) cubic pyrite (Py–II) associated with Sp–II is intergrown with dolomite–II (Dol–II).

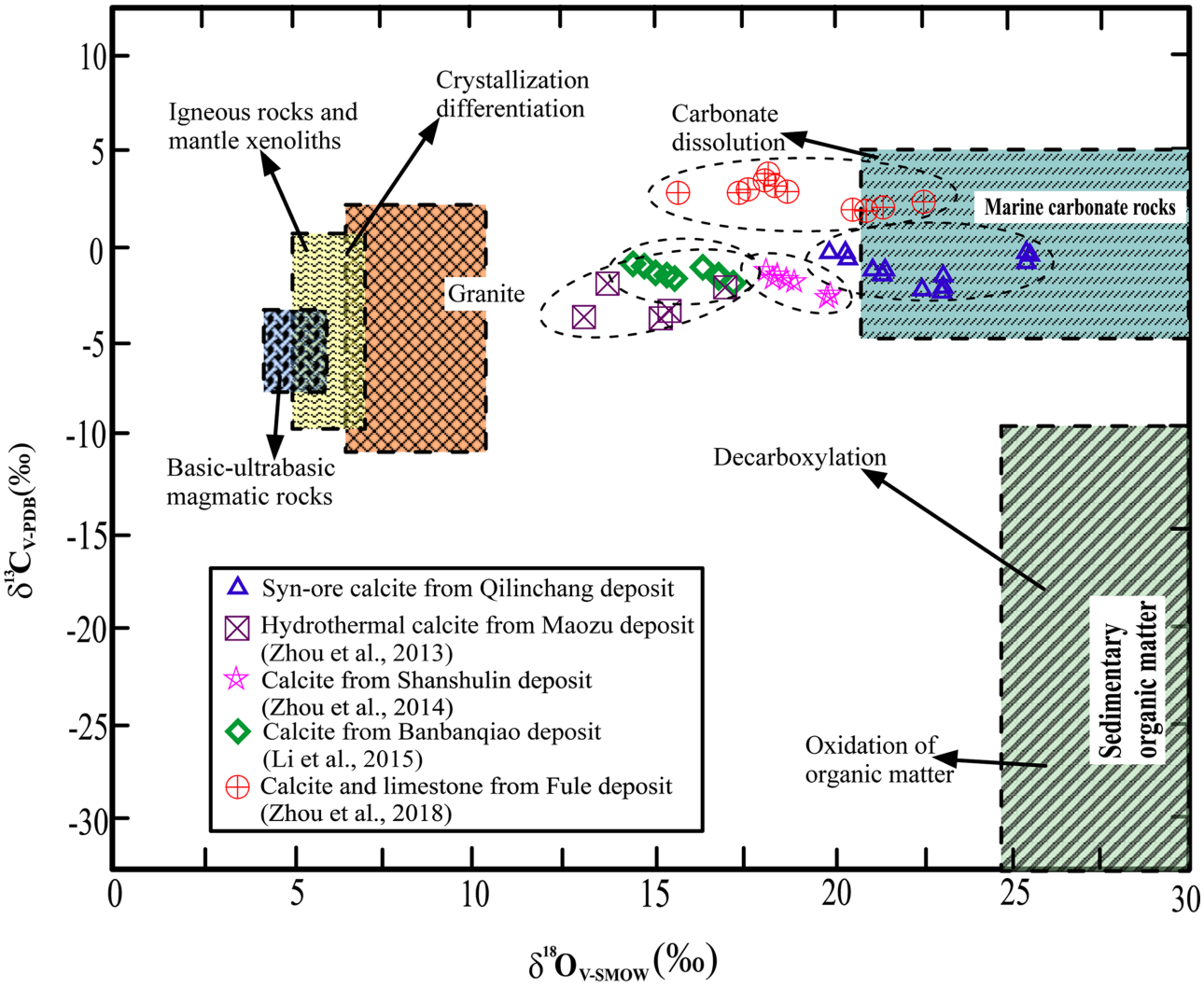

Figure 11. Plot of $\delta^{13}C_{V\text{–}PDB\ versus}\ \delta^{18}O_{V\text{–}SMOW}$ showing the isotopic composition of the syn–ore calcite from the Qilinchang Pb–Zn deposit, together with $\delta^{13}C_{V\text{–}PDB\ versus}\ \delta^{18}O_{V\text{–}SMOW}$ values of the Maozu, Shanshulin, Banbanqiao and Fule deposits, taken from (Zhou et al., 2013d, 2014; Li et al., 2015 and Zhou et al., 2018) respectively.

Table 1. Carbon and oxygen isotope compositions of syn–ore calcite samples from the Qilinchang ore deposit, Southwest China

Sample no.	Mineral/rock	Sample types	$\delta^{13}C_{PDB}$ (‰)	$2\sigma_m$	$\delta^{18}O_{SMOW}$ (‰)	$2\sigma_m$	$\delta^{18}O_{H2O}$ (‰)
HZ1	Stage II calcite	Syn–ore calcite	–2.01	0.04	+22.77	0.10	+13.27
HZ2	Stage II calcite	Syn–ore calcite	–2.06	0.04	+22.71	0.09	+13.21
HZ5	Stage II calcite	Syn–ore calcite	–2.35	0.04	+23.70	0.11	+14.20
HZ6	Stage II calcite	Syn–ore calcite	–2.19	0.04	+22.34	0.10	+12.84
HZ7	Stage II calcite	Syn–ore calcite	–1.71	0.08	+20.86	0.17	+11.36
HZ8	Stage II calcite	Syn–ore calcite	–1.74	0.05	+21.32	0.15	+11.82
HZ9	Stage II calcite	Syn–ore calcite	–1.65	0.07	+21.52	0.16	+12.02
HZ10	Stage II calcite	Syn–ore calcite	–0.44	0.05	+26.60	0.13	+17.10
HZ11	Stage II calcite	Syn–ore calcite	–0.39	0.05	+26.83	0.16	+17.33
HZ12	Stage II calcite	Syn–ore calcite	–0.37	0.04	+26.74	0.12	+17.24
HZ20	Stage II calcite	Syn–ore calcite	–0.61	0.05	+20.71	0.13	+11.21
HZ23	Stage II calcite	Syn–ore calcite	–1.97	0.04	+20.78	0.11	+11.28
HZ24	Stage II calcite	Syn–ore calcite	–1.21	0.05	+19.24	0.14	+9.74

$\delta^{18}O_{SMOW} = 1.03091 \times \delta^{18}O_{PDB} + 30.91$ (Coplen et al., 1983); $\Delta^{18}O_{Cal\text{–}H2O} = \delta^{18}O_{Cal} - \delta^{18}S_{H2O} = 2.78 \times 10^6/(t + 273.15)^2 - 2.89$, $t = 200^0C$ (Zheng and Chen 2000).

to –0.37‰ (average –1.44‰) and +19.24‰ to +26.83‰ (average +22.78‰), respectively. In comparison with similar deposits of Maozu (Zhou et al., 2013d), Shanshulin (Zhou et al., 2014), Banbanqiao (Li et al., 2015) and the recently studied Fule deposit (Zhou et al., 2018), all in the SYG province. The calcite extracts from the Qilinchang deposit have similar $\delta^{13}C_{PDB}$ values compared to other deposits except for the Fule deposit. Also, the values of the $\delta^{18}O_{SMOW}$ are slightly higher than all compared deposits.

Sulfur

The $\delta^{34}S_{CDT}$ values of sulfide extract from the ore stage samples of the Qilinchang deposit are presented in Table 2 and plotted in Fig. 12a. The $\delta^{34}S_{CDT}$ values of pyrite range from 13.36‰ to 16.36‰ (mean= 14.98‰; number of analyses (n)=13), galena samples have $\delta^{34}S_{CDT}$ values from 13.50‰ to 15.30‰ (mean=14.38‰, n=6), and sphalerite-I and sphalerite-II samples also have $\delta^{34}S_{CDT}$ values from 12.61‰ to 17.01‰ (mean=15.19‰, n=22) and 12.32‰ to 16.59‰ (mean=14.21‰, n=33), respectively. The $\delta^{34}S_{CDT}$ values of sulfide separates represent the total sulfur isotopic compositions of the ore-forming fluids, i.e., $\delta^{34}S_{\Sigma S} \approx \delta^{34}S_{sulfide}$. It is clear that the sulfides from the ore stage in the deposit are enriched in heavy sulfur and have $\delta^{34}S_{CDT}$ narrow range from 12.33‰ to 17.01‰, which is perceptibly different from mantle-derived sulfur with a $\delta^{34}S_{CDT}$ value of about 0‰. It is imperative to note

Table 2. Sulfur isotope compositions of sulfides samples from the Qilinchang deposit, Southwest China

Sample no.	Mineral	$\delta^{34}S_{VCDT}$ (‰)	Sample no.	Mineral	$\delta^{34}S_{VCDT}$ (‰)
HZQ-7-11a	Pyrite	16.36	HZQ-7-8	Sphalerite-I	13.58
HZQ-8-1a	Pyrite	14.13	HZQ-7-11b	Sphalerite-I	16.30
HZQ-3-10	Pyrite	16.13	HZQ-3-12	Sphalerite-I	15.76
HZQ-8-2	Pyrite	13.36	HZQ-DL26	Sphalerite-I	12.61
HZQ-3b	Pyrite	15.43	HZQ-8	Sphalerite-II	12.32
HZQ-14-2a	Pyrite	13.98	HZQ-4	Sphalerite-II	13.74
HZQ-11g	Pyrite	15.82	HZQ-8-1b	Sphalerite-II	13.91
HZQ-13d	Pyrite	13.54	HZQ-8-3	Sphalerite-II	13.45
HZQ-11c-1	Pyrite	16.27	HZQ-13-8	Sphalerite-II	15.13
HZQ-8-7	Pyrite	13.83	HZQ-7-1	Sphalerite-II	13.63
HZQ-3-9	Pyrite	16.24	HZQ-7-2	Sphalerite-II	14.34
HZQ-7-10a	Pyrite	15.60	HZQ-7-3	Sphalerite-II	14.19
HZQ-8-8	Pyrite	14.03	HZQ-4-1	Sphalerite-II	13.87
HZQ-13-7	Galena	15.30	HZQ-8-6	Sphalerite-II	13.68
HZQ-7-9a	Galena	13.50	HZQ-11c-2	Sphalerite-II	16.59
HZQ-13c	Galena	14.31	HZQ-13-5	Sphalerite-II	15.30
HZQ-13-10	Galena	14.20	HZQ-13-6	Sphalerite-II	15.84
HZQ-13-16	Galena	14.43	HZQ-4-2	Sphalerite-II	14.36
HZQ-13a	Galena	14.52	HZQ-3-14	Sphalerite-II	14.01
HZQ-13-13	Sphalerite-I	15.07	HZQ-9	Sphalerite-II	14.08
HZQ-11f	Sphalerite-I	17.01	HZPL03-8	Sphalerite-II	12.82
HZQ-3d	Sphalerite-I	15.82	HZQ-7-7	Sphalerite-II	13.57
HZQ-3-6	Sphalerite-I	15.83	HZQ-7a	Sphalerite-II	13.81
HZQ-3-4	Sphalerite-I	14.35	HZQ-5-1	Sphalerite-II	15.27
HZQ-4-5	Sphalerite-I	13.87	HZQ-4-9	Sphalerite-II	13.88
HZQ-7-12	Sphalerite-I	16.94	HZQ-14-2b	Sphalerite-II	13.71
HZQ-13-11	Sphalerite-I	15.94	HZQ-4-10	Sphalerite-II	14.21
HZQ-14-6	Sphalerite-I	15.38	HZQ-DL27	Sphalerite-II	12.79
HZQ-4-12	Sphalerite-I	13.52	HZQ-4-3	Sphalerite-II	14.45
HZQ-3-7	Sphalerite-I	15.72	HZQ-4-6	Sphalerite-II	13.62
HZQ-4-11	Sphalerite-I	13.34	HZQ-7-4	Sphalerite-II	14.30
HZQ-11e	Sphalerite-I	16.09	HZQ-3a	Sphalerite-II	15.29
HZQ-11i	Sphalerite-I	16.28	HZQ-7-10b	Sphalerite-II	16.11
HZQ-7-9b	Sphalerite-I	14.62	HZQ-3c	Sphalerite-II	15.48
HZQ-7-13	Sphalerite-I	16.19	HZQ-4-7	Sphalerite-II	13.67
HZQ-7-14	Sphalerite-I	16.28	HZQ-4-8	Sphalerite-II	13.27
HZQ-13b	Sphalerite-I	13.73	HZQ-4b	Sphalerite-II	14.15

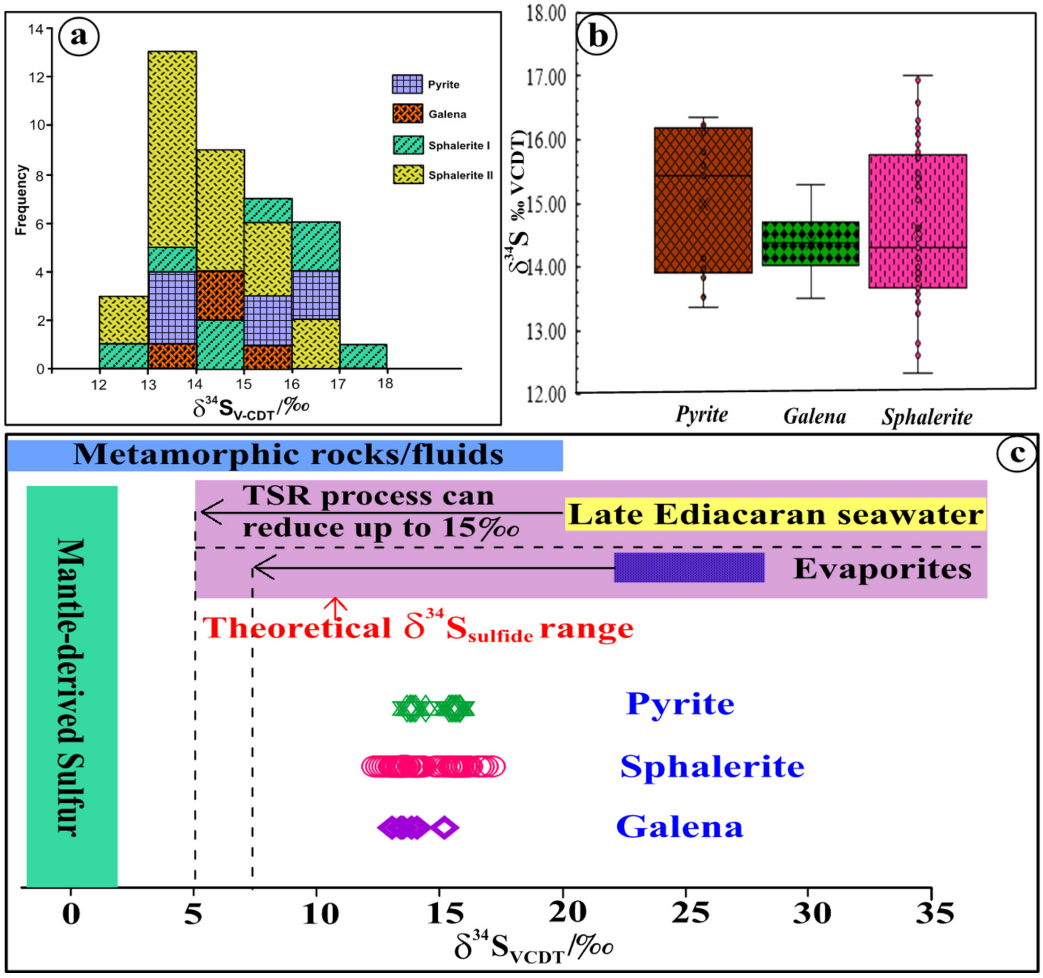

Figure 12. (a) Sulfur isotope composition histogram of sulfides of the Qilinchang Pb–Zn deposit; (b) Box plot of $\delta^{34}S$ values for pyrite, galena, and sphalerite, the sulfur isotope compositions shown are isotopically relatively homogenous and consistent with global Carboniferous seawater sulfate with average composition of 14.98‰ for pyrite, 14.38‰ for galena and 14.60‰ for sphalerite; (c) Sulfur isotope ratio diagram comparing $\delta^{34}S$ values of pyrite, sphalerite, and galena with mantle-derived Sulfur, late Ediacaran seawater, and evaporites.

that from pyrite to sphalerite and then to galena, the $\delta^{34}S_{CDT}$ values are decreasing (Fig. 12b, c), indicating a sulfur isotope equilibrium fractionation, which is a function of temperature and relative metal-sulfide bond strengths.

Lead

The lead isotopic data of the sulfide extracts from the ore stage samples of the Qilinchang deposit are shown in Table 3 and plotted in Fig. 13 and 14. The lead isotope compositions of galena and sphalerite are homogenous with galena having $^{206}Pb/^{204}Pb$, $^{207}Pb/^{204}Pb$, and $^{208}Pb/^{204}Pb$ ratios range from 18.503-18.506, 15.758-15.760, and 39.024-39.036 and an average of 18.505, 15.759, and 39.032, respectively. The sphalerite-I samples also have a similar trend of lead isotopic data of $^{206}Pb/^{204}Pb$, $^{207}Pb/^{204}Pb$, and $^{208}Pb/^{204}Pb$ ratios range from 18.493-18.505, 15.755-15.759, and 39.002-39.025 with a mean value of 18.500, 15.757, and 39.013, respectively. Also, lead isotopic ratios of sphalerite-II are as follows: $^{206}Pb/^{204}Pb$, $^{207}Pb/^{204}Pb$, and $^{208}Pb/^{204}Pb$ ratios range from 18.492-18.507, 15.754-15.758, and 38.996-39.030 and an average of 18.496, 15.756, and 39.008, respectively.

REE Concentrations

The REE compositions of syngenetic calcite and primary sulfide are presented in Fig. 15 and S1. Twelve calcite samples have total REE (∑REE, Y not included) concentrations ranging from 5.43 ppm to 27.52 ppm (average 11.88 ppm), δEu values ranging from 0.56 to 0.70 (average 0.62), and La_N/Yb_N elemental ratios ranging from 3.03 to 11.39 (average 7.58). The sulfide samples include six pyrite extracts having ∑REE concentrations ranging between 0.39 ppm to 0.87 ppm (average 0.62 ppm), δEu values range between 0.51 to 2.14 (average 1.04), and La_N/Yb_N ratios ranging from 0.67 to 9.83 (average 3.20). Also, four galena extracts have ∑REE values from 0.02 ppm to 0.22 ppm (average 0.09 ppm), δEu values of galena range from 0.05 to 0.62 (average 0.38), and La_N/Yb_N ratios ranging from 1.55 to 10.16 (average 4.34). Eight sphalerite separates have ∑REE values ranging from 0.02 ppm to 1.00 ppm (average 0.54 ppm), δEu values range between 0.38 to 1.60 (average 0.80), and La_N/Yb_N ratios ranging from 2.13 to 8.38 (average 4.33). It is clearly noted that the calcite has higher REE concentrations compared to the sulfide. Also, a negative Eu anomaly is observed in all the analyzed samples.

Table 3. Lead isotope compositions of sulfides samples from the Qilinchang deposit, Southwest China

Sample number	Mineral	$^{208}Pb/^{204}Pb$	2σ	$^{207}Pb/^{204}Pb$	2σ	$^{206}Pb/^{204}Pb$	2σ
HZQ–13–7	Galena	39.024	0.002	15.758	0.001	18.503	0.001
HZQ–7–9a	Galena	39.035	0.003	15.760	0.001	18.506	0.001
HZQ–13c	Galena	39.030	0.002	15.759	0.001	18.505	0.001
HZQ–13–10	Galena	39.033	0.002	15.759	0.001	18.505	0.001
HZQ–13–16	Galena	39.035	0.002	15.760	0.001	18.506	0.001
HZQ–13a	Galena	39.036	0.002	15.760	0.001	18.506	0.001
HZQ–11f	Sphalerite-I	39.023	0.002	15.757	0.001	18.502	0.001
HZQ–7–12	Sphalerite-I	39.011	0.001	15.755	0.000	18.500	0.000
HZQ–13–11	Sphalerite-I	39.012	0.002	15.755	0.001	18.500	0.001
HZQ–4–12	Sphalerite-I	39.002	0.002	15.756	0.001	18.493	0.001
HZQ–11e	Sphalerite-I	39.010	0.002	15.756	0.001	18.499	0.001
HZQ–11i	Sphalerite-I	39.013	0.002	15.756	0.001	18.501	0.001
HZQ–7–9b	Sphalerite-I	39.022	0.002	15.757	0.001	18.504	0.001
HZQ–7–13	Sphalerite-I	39.011	0.002	15.757	0.001	18.500	0.001
HZQ–7–14	Sphalerite-I	39.011	0.002	15.756	0.001	18.501	0.001
HZQ–13b	Sphalerite-I	39.025	0.002	15.759	0.001	18.505	0.001
HZQ–7–8	Sphalerite-I	39.010	0.002	15.758	0.001	18.496	0.001
HZQ–7–11b	Sphalerite-I	39.006	0.001	15.756	0.001	18.498	0.001
HZQ–7–1	Sphalerite-II	39.007	0.002	15.758	0.001	18.496	0.001
HZQ–4–1	Sphalerite-II	39.004	0.002	15.757	0.001	18.493	0.001
HZQ–8–6	Sphalerite-II	39.011	0.002	15.758	0.001	18.496	0.001
HZQ–13–5	Sphalerite-II	39.026	0.002	15.758	0.001	18.505	0.001
HZQ–3–14	Sphalerite-II	39.030	0.002	15.756	0.001	18.507	0.001
HZQ–7–7	Sphalerite-II	39.007	0.002	15.757	0.001	18.495	0.001
HZQ–7a	Sphalerite-II	39.002	0.002	15.756	0.001	18.494	0.001
HZQ–5–1	Sphalerite-II	39.008	0.002	15.756	0.001	18.497	0.001
HZQ–DL27	Sphalerite-II	38.998	0.002	15.755	0.001	18.492	0.001
HZQ–7–4	Sphalerite-II	38.996	0.002	15.754	0.001	18.492	0.001
HZQ–4–7	Sphalerite-II	39.001	0.003	15.756	0.001	18.494	0.001
HZQ–4b	Sphalerite-II	38.999	0.002	15.755	0.001	18.492	0.001

Discussion

Nature and Source of the Ore-forming Fluids

Insights from C-O Isotopes

Conventionally, carbon species in hydrothermal fluids may originate from these processes; (a) a magmatic source (igneous rocks and mantle xenoliths, basic-ultrabasic magmatic rocks and granite) (Taylor et al., 1967), (b) oxidation of reduced carbon species in rocks (organic compounds in sedimentary rocks, graphite in igneous and metamorphic rocks) (Veizer and Hoefs, 1976), and (c) leaching of sedimentary carbonates (Ohmoto and Rye, 1979; Liu and Liu, 1997). During fractionation of carbon isotopes, the $\delta^{13}C$ values of carbonate minerals is a function of the following; (a) temperature; (b) $\delta^{13}C_{\Sigma C}$ (which varies with the source of the fluid and can have very negative values; (c) the ratio of the various carbon species due to the large isotopic fractionations between the oxidized and reduced species; i.e., CO_2 and CH_4); (d) geochemical parameters, such as temperature, pH and fO_2 (Ohmoto, 1972; Ohmoto and Rye, 1979). Typical ranges of C and O isotopic compositions in geologic systems have been documented, the $\delta^{13}C$ and $\delta^{18}O$ values for mantle-derived CO_2 range between –8 to –4‰ and +6 to +10‰ (Taylor et al., 1967), respectively, typical marine carbonate rocks have $\delta^{13}C$ values of –4 to +4‰, and $\delta^{18}O$ values of +20 to +30‰ (Veizer and Hoefs, 1976) and sedimentary organic matters have $\delta^{13}C$ range from –30 to –10‰ and $\delta^{18}O$ from +24 to +30‰ (Liu and Liu, 1997; Hoefs, 2009). The $\delta^{13}C_{PDB}$ values (–2.35 to –0.37‰, with an average of –1.44‰) of syn-ore calcite samples from the Qilinchang deposit exceeded that of the sedimentary organic matter, and adjacent mantle-derived rocks but are comparable with that of marine carbonate rocks (Fig. 11). The $\delta^{18}O_{SMOW}$ values (+19.24 to 26.83‰, average of 13.28‰) of syn-ore calcite extracts from the Qilinchang deposit are significantly greater than that of the mantle-derived rocks (+6.0 to +10.0‰; Taylor et al., 1967), but most values are analogous to the marine carbonate rocks (+20.0 to +30.0‰; Veizer and Hoefs, 1976) and lesser than the sedimentary organic matter (+24.0 to +35.0‰; Liu and Liu, 1997). Contrastingly, the calculated $\delta^{18}O_{H2O}$ values (+9.74 to +17.33, average of +13.28‰) based on oxygen isotope equilibrium fractionation

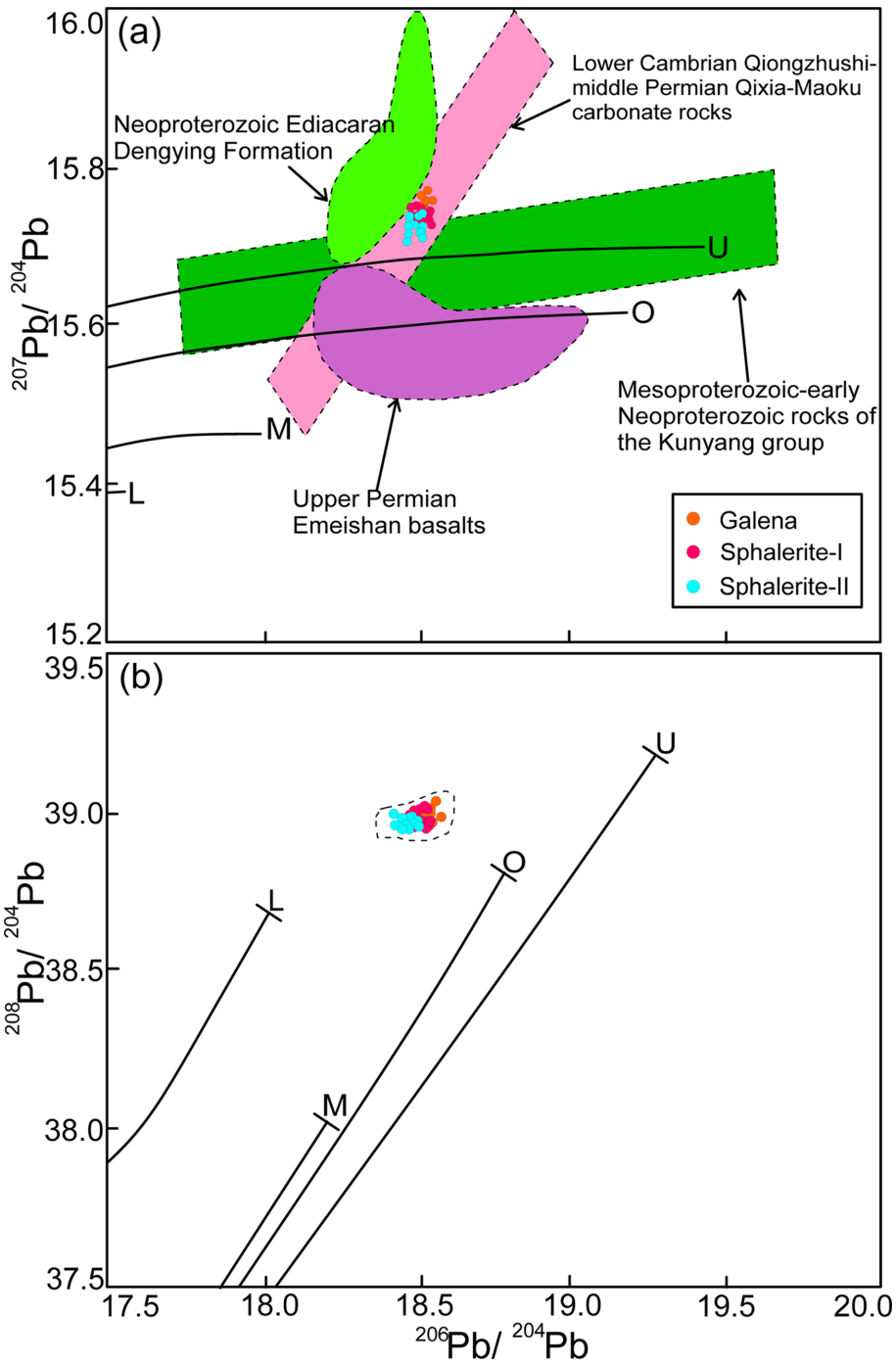

Figure 13. Plots of (a) $^{206}Pb/^{204}Pb$ vs. $^{207}Pb/^{204}Pb$ and, (b) $^{206}Pb/^{204}Pb$ vs. $^{208}Pb/^{204}Pb$ for galena and sphalerite. Note: U–Upper crust, O–Orogenic belt, M–Mantle, and L–Lower crust (Zartman and Doe 1981). Coloured fields data taken from Zheng and Wang, 1991; Wang et al., 2000; Zhou et al., 2001; Han et al., 2007 and Yan et al., 2007.

between calcite and water ($\Delta^{18}O_{Cal\text{-}H2O} = \delta^{18}O_{Cal}\text{-}\delta^{18}S_{H2O} = 2.78 \times 10^6/(t + 273.15)^2 - 2.89$, t = 200°C (Zheng and Chen, 2000) are lower than those of sedimentary organic matters, marine carbonate rocks, but are analogous to those of mantle or metamorphic fluids having documented values of +2 to + 25‰ (Hoefs, 2009). Inference can be made that the mantle and organic matters did not contribute a substantive amount of carbon to the hydrothermal fluids and suggested that the carbon in the fluids was probably injected by the carbonate host rocks of the Carboniferous Baizuo Formation (Han et al., 2007; Zhang et al., 2017). Also, based on (Fig. 11), syn-ore calcite samples from the Qilinchang deposit plotted in the field of marine carbonate rocks, but noticeably far from the sedimentary organic matter field. This is an indication that the ore-forming fluids were related to water/rock (W/R) interaction between the mantle and/or metamorphic fluids and carbonates. The values obtained from this study are consistent with previous data of host rock and miarolitic calcites (Huang et al., 2003; Zhang et al., 2005b; Han et al., 2007; Zhang et al., 2017) but different from the primary ore calcites. The correlation between $\delta^{13}C_{V\text{-}PDB}$ and $\delta^{18}O_{V\text{-}SMOW}$ is slightly negative (Fig. 11). Deciphering if the CO_2 present in the hydrothermal fluids were generated from the mantle, the evolved calcite would display constant $\delta^{13}C_{V\text{-}PDB}$ values with elevated $\delta^{18}O_{V\text{-}SMOW}$ values. Also, if the CO_2 is from the marine carbonate, the precipitated calcite will have constant $\delta^{13}C_{V\text{-}PDB}$ values with a decrease in $\delta^{18}O_{V\text{-}SMOW}$ values. This expression between $\delta^{13}C_{V\text{-}PDB}$ and $\delta^{18}O_{V\text{-}SMOW}$ values shows that CO_2 in the ore-forming fluids was sourced neither from the mantle, marine carbonate nor from the sedimentary organic matters. Similarly, the depletion of ^{18}O in the ore-forming fluids compared to the carbonate host rocks and was likely to be derived from a mixed source region (mantle-derived oxygen in the Emeishan basalts and dissolved oxygen from the carbonate host rocks). Therefore, we postulate that the $\delta^{18}O$ isotope fingerprint was generated by the water-rock interplay between two mixed fluids (deep-seated fluids and subsurface brine leached from carbonate wall rocks) and carbonates.

Source of Sulfur and Sulfate Reduction Mechanisms

The presence of sulfur in sedimentary and hydrothermal mineral deposits, which generally occurred as sulfide ± sulfate minerals, may originate from any of these processes; (a) an igneous source (magmatic fluids and magmatic sulfur-rich minerals; $\delta^{34}S \approx 0‰$); (b) seawater sulfate (in connate water trapped in marine sediments or meteoric water as sulfate dissolved from marine evaporites; $\delta^{34}S \approx 20‰$). Mantle-derived sulfur usually shows a narrow range of $\delta^{34}S$ values with a mean close to 0‰; this has been deciphered to have formed from magmatic fluids. Whereas, mineral deposits in which the sulfides showed a wide range but mostly negative $\delta^{34}S$ values were interpreted as originated from sedimentary or biogenic because at low temperatures bacterial reduction of sulfate is the most effective mechanism of

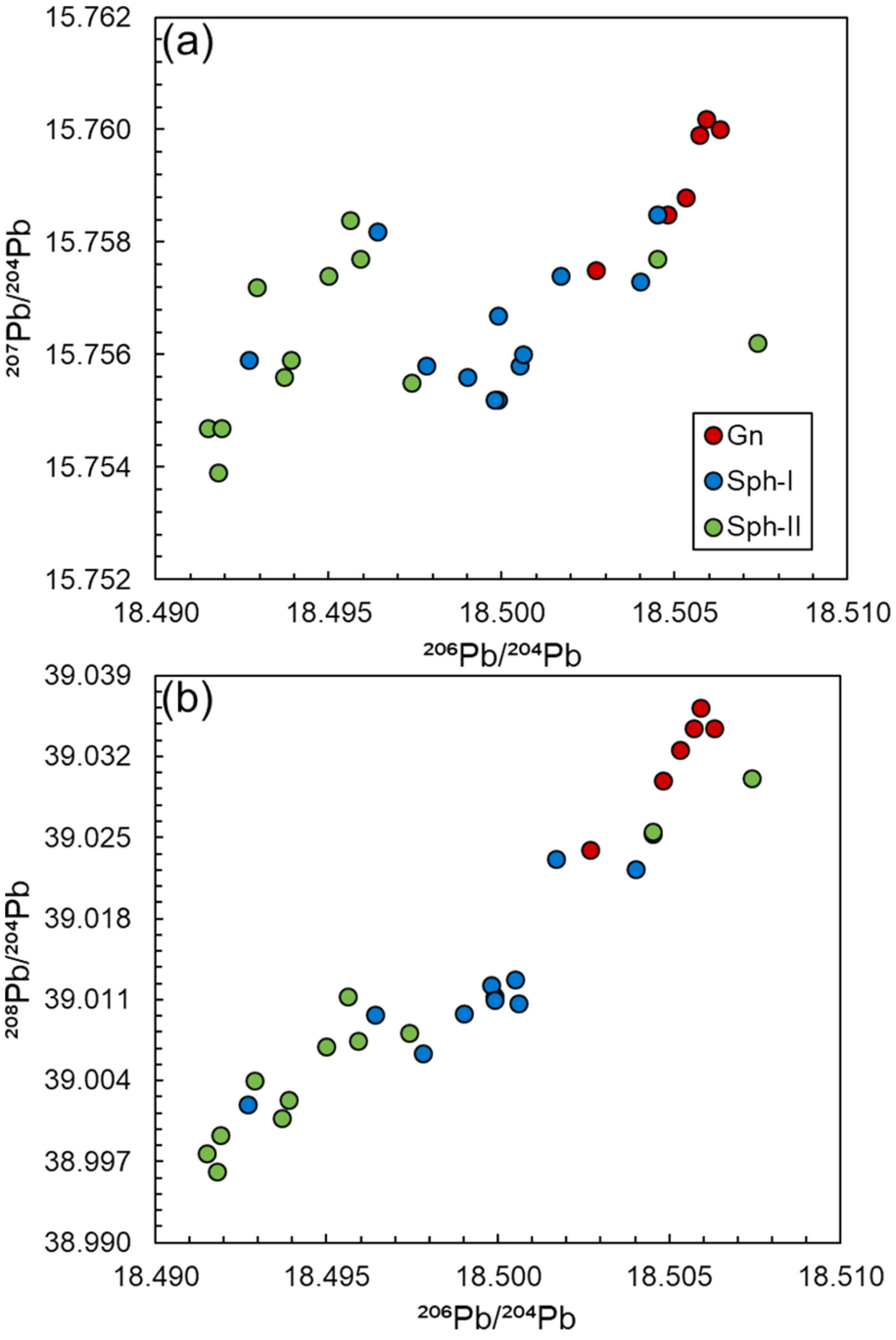

Figure 14. Plots of (a) $^{207}Pb/^{204}Pb$ vs. $^{206}Pb/^{204}Pb$ and (b) $^{208}Pb/^{204}Pb$ vs. $^{206}Pb/^{204}Pb$ exhibiting a gradually increase in Pb isotopic ratios from sphalerite to galena.

sulfur depletion in the sulfides (Ohmoto, 1972; Rye and Ohmoto, 1974; Claypool et al., 1980; Liu and Lin, 1999; Seal, 2006). Sulfide ores in the Qilinchang deposit have an occurrence of oxidized, unoxidized, simple sulfur-bearing minerals assemblage of pyrite, sphalerite, and galena (Han et al., 2007). The obtained $\delta^{34}S_{CDT}$ values of seventy-four sulfide samples are presented in Table 2 and plotted in Fig. 12a. The $\delta^{34}S_{CDT}$ values range from +12.33 to 17.01‰ (average 14.65‰) of which pyrite, sphalerite-I, sphalerite-II, and galena have $\delta^{34}S_{CDT}$ values range from 13.36 to 16.36‰, 12.61 to 17.01‰, 12.32 to 16.59‰, and 13.50 to 15.30‰, respectively (Fig. 12c). The $\delta^{34}S$ values of the sulfide minerals indicate that the relations of $\delta^{34}S_{pyrite} > \delta^{34}S_{sphalerite} > \delta^{34}S_{galena}$ and implies that sulfide precipitated under sulfur isotope equilibrium fractionation. $\delta^{34}S$ values (Table 2) of pyrite, sphalerite, and galena are consistent with that of the global Carboniferous seawater sulfate (15-20‰; Thode, 1970; Claypool et al., 1980; Hoefs, 1987), indicating that sulfur was derived predominantly from evaporite rocks within the strata. Also, previously published bulk $\delta^{34}S$ data for pyrite, sphalerite, and galena (Li et al., 2006) show similar feature for equilibrium fractionation of S isotopes, with the ores profoundly enriched in sulfur (10.9‰ to 17.4‰), suggesting that the sulfur in the ore-forming fluids had reached isotopic equilibrium. Much of the sulfides in the Qilinchang deposit appear to have precipitated in isotopic equilibrium at a temperature above 100°C from ore-forming fluids with a $\delta^{34}S$ average value of 14.65‰, postulating that the ore-forming fluids derived both metals and reduced sulfur from deep sedimentary basins and migrated through the carbonate strata of various ages. These observations also indicate that S^{2-} in the hydrothermal fluids originated by thermal-chemical sulfate reduction (TSR) within the evaporites (Han et al., 2007; Pass et al., 2014). This study of the $\delta^{34}S$ composition of sulfide minerals from the Qilinchang deposit confirmed that reduced sulfur in the basinal fluids was derived from evaporites in the host strata at temperatures ranging from 164 to 221°C (Han et al., 2007) producing H_2S-rich fluid by thermochemical sulfate reduction with restricted inducement from mantle-derived sulfur.

Source of Metals

Radiogenic lead isotopes are produced by constant radioactive decay of unstable elements of uranium (U) and thorium (Th). The applications of lead isotope ratios to studies of mineral deposits have been widely adopted which include: (a) determination of age and chronological history of the deposits; (b) unravel the source of lead; (c) providing information on geochemistry of U, Th and Pb in the upper crust and mantle; and (d) useful in exploration of mineral deposits. Conventionally, sulfide minerals have very low U/Pb and Th/Pb ratios alternatively referred to as *common lead*; this is due to its constant isotopic composition, which does not appreciably change with time (Zartman and Doe, 1981; Pass et al., 2014). The obtained Pb isotopic data from galena and sphalerite-I&II (Table 3) are homogenous. The analytical data are plotted in Fig. 13 with $^{206}Pb/^{204}Pb$ vs. $^{207}Pb/^{204}Pb$ (Fig. 13a) and $^{206}Pb/^{204}Pb$ vs. $^{208}Pb/^{204}Pb$ (Fig. 13b) ratios within the analytical uncertainty (2σ). Based on the growth curves of isotopic Pb, the $^{206}Pb/^{204}Pb$ vs. $^{207}Pb/^{204}Pb$ and the $^{206}Pb/^{204}Pb$ vs. $^{208}Pb/$

^{204}Pb ratios plot above the Pb evolution curve of average upper continental crust (Fig. 13) (Zartman and Doe, 1981), suggesting that the Pb sources for galena and sphalerite are similar and predominantly originated from basement rocks.

Also, based on the plumbotectonics plot for the growth curves of isotopic Pb ^{206}Pb/^{204}Pb vs. ^{207}Pb/^{204}Pb and field plots of previous data namely: the Neoproterozoic Ediacaran Dengying Formation, Lower Cambrian Qiongzhushi-Middle Permian Qixia-Maoku carbonate rocks, Mesoproterozoic to early Neoproterozoic rocks of the Kunyang Group and the Upper Permian Emeishan basalts (Zheng and Wang, 1991; Wang et al., 2000; Zhou et al., 2001; Han et al., 2007; Yan et al., 2007), these values plot within the Pb isotope field of basement rocks of the Kunyang Group indicating the main source of the metals for the Qilinchang Pb-Zn deposit.

As observed in Fig. 13a, the Pb data for the Lower Cambrian to Middle Permian carbonate rocks overlaps the data for the analyzed ores; this suggests that there is no single source for the Pb as the source can also be related to the Pb in the Cambrian to Permian strata. This is similar to previous findings of Bao et al., 2017, suggesting that the basement rocks of the Kunyang Group are the primary source of the ore metals, but the Proterozoic igneous rocks and Precambrian gneisses can also contribute to the ore deposition. Taking into account the increased values in the ^{206}Pb/^{204}Pb and ^{208}Pb/^{204}Pb ratios from sphalerite to galena (Fig. 14a-b) which is attributed to elevated ^{206}Pb/^{204}Pb and ^{208}Pb/^{204}Pb-enriched fluid given more Pb to galena than sphalerite and also variation in the U and Th contents (lower U and Th in sphalerite compared to galena). From all these indications, it can be suggested that the formation of the Qilinchang deposit was initiated with interactions between deep circulating fluids moving upward within thick ore metal-rich clastic rocks and host Lower Cambrian to Middle Permian carbonate rocks extracting ores to form the deposit.

Constraint from Rare Earth Elements

Geochemically, the REE are relatively electropositive, and as a result, they generally form ionic compounds. Mineralogically, the REE, therefore, forms oxides, carbonates, silicates, halides, and phosphates but not sulfides (Gupta and Krishnamurthy, 2005). The compositions of REE in sulfide minerals are mostly controlled by the initial composition of the parental fluid and physical-chemical behaviour of the lanthanide group (e.g., oxidation state, temperature, pH, and Eh) of the depositional environment of sulfide minerals (Platt, 2012). The sulfides from the ore-stage mineralization of the Qilinchang deposit have low ∑REE contents compared to the calcite (S1). The ∑REE concentration of the calcite (Fig. 15a) represents the approximate ∑REE of the hydrothermal fluids. The samples display weakly negative Eu anomalies (δEu > 1), except for pyrite (Fig. 15b). Considering the REE chondrite-normalized patterns (Fig. 15), the pyrite (Fig. 15b), galena (Fig. 15c),

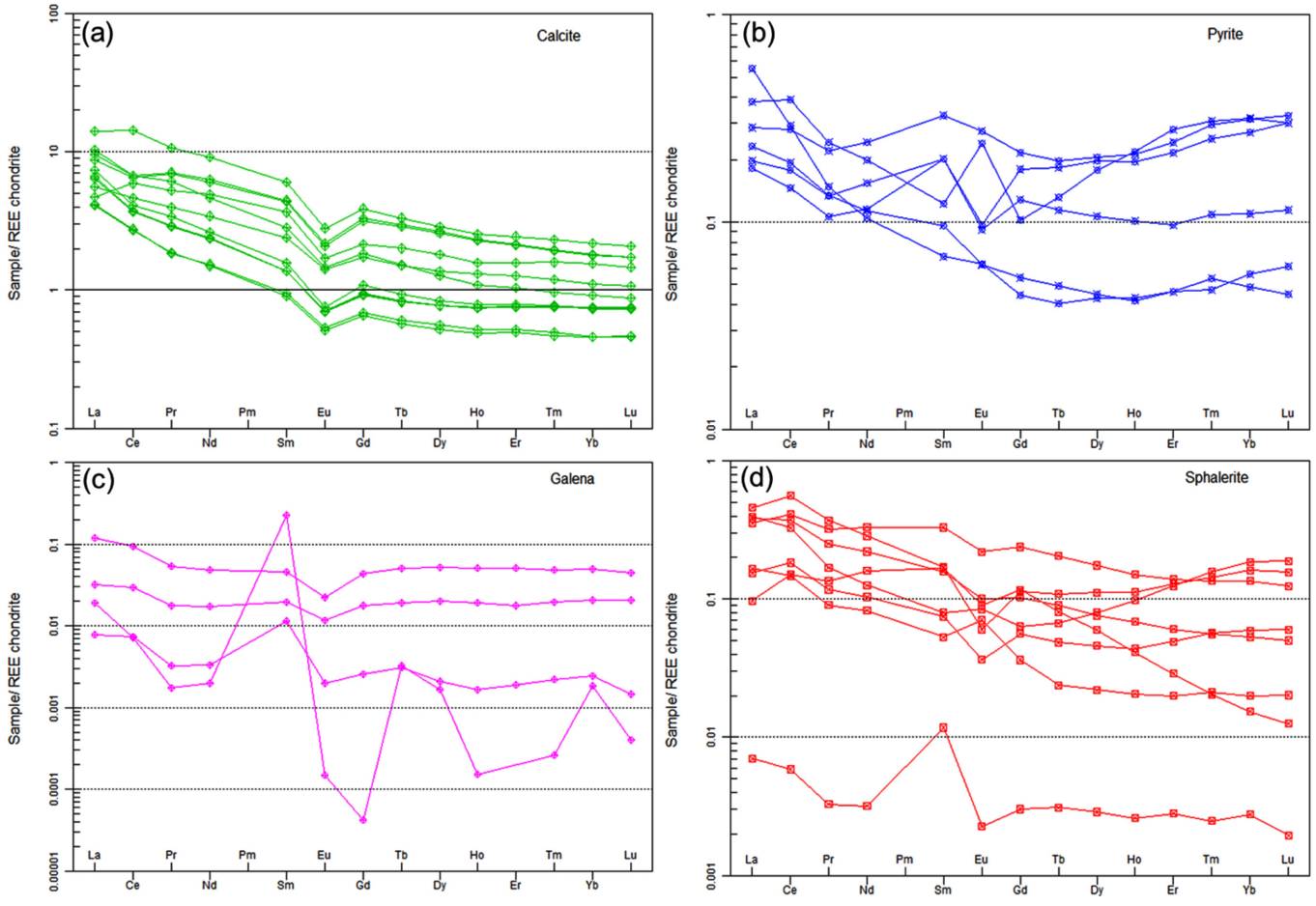

Figure 15. Chondrite–normalized REE patterns (Boynton, 1984). (a) REE pattern for calcite; (b) REE pattern for pyrite; (c) REE pattern for galena; (d) REE pattern for sphalerite.

and sphalerite (Fig. 15d) show similar patterns but slightly different from those of calcite (Fig. 15a). Negative Eu anomalies typically occur in hydrothermal fluids at lower temperatures below 200°C due to the depletion of Eu (II) in the fluids. Consequently, the δEu values of calcite, galena, and sphalerite (average δEu = 0.62, 0.38, and 0.80 respectively) are lesser than 1, suggesting that the fluids were Eu-depleted or interacted with negative Eu anomaly-bearing minerals. The regular pattern of REE in calcite and negative Eu anomalies indicates that the input of REEs in the fluids was probably sourced from carbonate host rocks.

Age of Mineralization

Previous investigations have utilized the application of Sm-Nd isotopic studies of hydrothermal calcite from the Kuanshanchang and Qilinchang orebodies in the Huize Pb-Zn deposit and attained isochron ages of 226 ± 15 Ma and 225 ± 38 Ma respectively (Li et al., 2004). Moreover, Zhang et al. (2005b) demonstrated that K-Ar isotopic dating of hydrothermal clay minerals from the Huize Pb-Zn deposit is feasible and attained the isochron age of 176.5 ± 2.5 Ma. Zhou et al. (2013a) also reported Rb-Sr isochron ages of 191.9 ± 6.9 Ma, 196 ± 13 Ma, and 200.1 ± 4.0 Ma (Lin et al., 2010) for sphalerite from the Tianqiao, Maozu and Paoma Pb-Zn deposits respectively. This geochronological technique has been applied broadly for certain sulfide minerals (Nakai et al., 1993; Christensen et al., 1995; Li et al., 2005). Ore-stage sphalerite samples from the Jinshachang deposit were analyzed using a modified single grain Rb-Sr isotopic dating method utilizing the high precision, extremely-low procedural blank TIMS, an isochron age of 206.8 ± 3.7 Ma was calculated (Zhou et al., 2015). Findings indicate that 1/Sr values do not co-vary with $^{87}Sr/^{86}Sr$ ratios, and hence the isochron age is not a pseudo-isochron and has an isochronal interpretation (Yin et al., 2009; Zhou et al., 2013b), so ca. 200 Ma is interpreted to be the main time of Pb-Zn mineralization in the SYG province. These conclusions are analogous to prior interpretations of Mao et al. (2012) applying Sm-Nd isotopic ages of fluorite concluded to be 201.1 ± 2.9 Ma and deliberated periods of magmatic events in the province evident by the Late Permian Emeishan basalt with K-Ar ages of 218.6-253.3 Ma (Han et al., 2007). Consequently, we posit that the Qilinchang and numerous deposits in the province are developed dominantly between 200-230 Ma corresponding to Late Triassic. These particular deposits depict robust correlation to the collision of the Yangtze Block with adjacent blocks associated with the closure of the Tethys Ocean (Carter et al., 2001; Zhang et al., 2006; Reid et al., 2007; Hu et al., 2017), also known as the Indosinian Orogeny.

Genetic Model

From this current study, the nature of the fluid type (basinal brine), the source of sulfur (Carboniferous seawater sulfate and evaporite rocks within the strata) and the source of metals (Mesoproterozoic to early Neoproterozoic basement of the Kunyang Group) ore genesis model for the Qilinchang deposit is proposed (Fig. 16). Predicated on the geological and geodynamic setting of the SYG metallogenic province, it had been reported that multiple orogenic events occurred, especially in the Western Yangtze Platform (Zaw et al., 2007; Hu et al.,

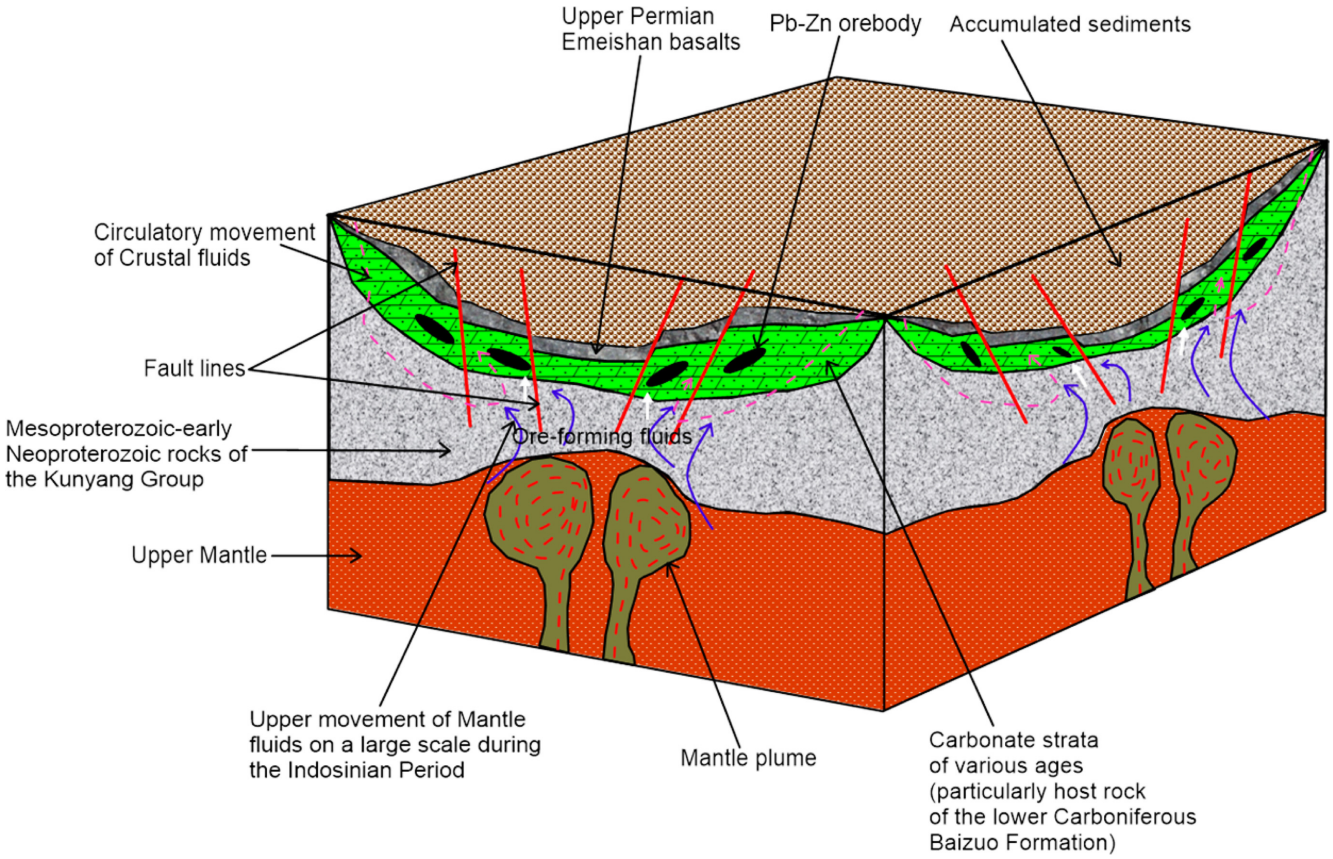

Figure 16. Ore genesis model for the Qilinchang Pb–Zn ore deposit.

2012, 2017). Amongst all several orogenic episodes which occurred in the SYG province is the amalgamation of South China during the early Proterozoic by the collision of the Yangtze and Cathaysian Blocks.

Sulfide mineralization in the Qilinchang deposit has no direct genetic link with the Permian Emeishan basalt; this had led previous researchers to classify the deposit as a Mississippi Valley-Type deposit (Han et al., 2007). This deposit displays a lot of features analogous to typical MVT Pb-Zn deposits in terms of deposit geology, tectonic setting, alteration processes, trace element, and isotope compositions. On the other hand, the ore bodies occur as massive, veined, disseminated, and brecciated forms, that are mainly stratabound; they are classified as stratabound-type of deposit. However, the Qilinchang deposit exhibits some unique geological and geochemical characteristics such as its peculiar ore features, homogenization temperatures of fluid inclusions, trace element contents, and involvement with magmatic heat. Also, the study of fluid inclusions in sphalerite and calcite indicate that the ore-forming fluids in the Qilinchang deposit are characterized by low to moderate temperatures (100-344°C) and salinities (6-12 wt.% NaCl equiv.) (Han et al., 2007). The occurrence of abundant Ag, Ge, In, Ga, Cd, and Tl of which Ag and Ge are economically mined having grades of 46-100 g/t and 30-81 g/t for Ag and Ge, respectively (Huang et al., 2003). The Ag grade and homogenization temperatures of fluid inclusions are quite different from typical MVT deposits (<~10 g/t Ag and <150°C) (Bonsall et al., 2011). Furthermore, the grades of the sulfide ores in the Qilinchang deposit (Pb+Zn: 25-35 wt.%) are higher than those of MVT deposits (usually <10 wt.%). The elemental composition of pyrite using the Co and Ni contents (Meng et al., 2019) shows that the Huize pyrite has lower contents compared to typical volcanogenic massive sulfide, porphyry copper and iron-oxide copper-gold deposits, arguably suggesting less or no involvement of a magmatic link with the Pb-Zn mineralization.

Wherefore, using the new results from the isotope systematics, we propose that the Qilinchang deposit does not have a direct genetic relationship with the Permian Emeishan basalt. However, we cannot dispute the involvement of magmatic heat. Therefore, due to the tectonic setting, ore body features, wall-rock alteration processes, and trace element composition, we regard the Qilinchang deposit as an exceptional type of deposit transiting between MVT and high-temperature carbonate-replacement Pb-Zn deposits.

Conclusions

The detailed integration of geological and mineralogical studies, systematic application of C-O-S-Pb isotopic data, and rare earth elements studies of the Qilinchang Pb-Zn deposit mainly hosted in the Lower Carboniferous Baizuo Formation was carried out to determine the sources of sulfur and metals, the mechanisms of ore precipitation and fluid evolution. Carbon and oxygen isotopic characteristics suggest that the ore-forming fluids were mainly derived from water-rock interaction between the mantle/metamorphic fluids and carbonates. The $\delta^{34}S$ of sulfides (+12.33 to +17.01‰) is related to the thermochemical reduction of Carboniferous seawater sulfate and are mainly derived from evaporites in the host strata producing H_2S-rich fluid by TSR with restricted inducement from mantle-derived sulfur. The homogenous composition of Pb isotopic data of galena and sphalerite indicates that the metals were predominantly originated from the basement rocks of the Mesoproterozoic-early Neoproterozoic rocks of the Kunyang Group and the Cambrian to Permian strata.

Acknowledgments

This research was jointly funded by the National Natural Science Foundation of China (Grant number: U1812402, 41830432) and the National 973 Program of China (Grant number: 2014CB440906). The first author is grateful to the Chinese Academy of Sciences and The World Academy of Sciences for sponsoring this research through the CAS-TWAS President's Fellowship programme.

References

Ali, J.R., Thompson, G.M., Zhou, M.F., and Song, X.Y., 2005, Emeishan large igneous province, SW China. Lithos, v. 79, pp. 475–489. doi:10.1016/j.lithos.2004.09.013.

Bao, Z., Li, Q., and Wang, C.Y., 2017, Metal source of giant Huize Zn–Pb deposit in SW China: New constraints from in situ Pb isotopic compositions of galena. Ore Geology Reviews, v. 91, pp. 824–836.

Bonsall, T.A., Spry, P.G., Voudouris, P.C., Tombros, S., Seymour, K.S., and Melfos, V., 2011, The geochemistry of carbonate–replacement Pb–Zn–Ag mineralization in the Lavrion district, Attica, Greece: Fluid inclusion, stable isotope, and rare earth element studies. Economic Geology, v. 106, pp. 619–651.

Boynton, W.V., 1984, Cosmochemistry of the rare earth elements: meteorite studies: In Developments in geochemistry, Elsevier, v. 2, pp. 63–114.

Brannon, J.C., Podosek, F.A., and McLimans, R.K., 1992, Alleghenian age of the Upper Mississippi Valley zinc-lead deposit determined by Rb–Sr dating of sphalerite. Nature, v. 356, pp. 509–511. doi:10.1038/356509a0.

Carter, A., Roques, D., Bristow, C., and Kinny, P., 2001, Understanding Mesozoic accretion in Southeast Asia: significance of Triassic thermotectonism (Indosinian Orogeny) in Vietnam. Geology, v. 29, pp. 211–214.

Chen, J., 1993, A discussion on the genesis and metallogenic model of the Qilinchang Zn–Pb–(Ag) sulfide deposit. Journal of Nonferrous Mineral Resources and Exploration, v. 2, pp. 85–90 (in Chinese with English abstract).

Chen, M.H., Mao, J.W., Li, C., Zhang, Z.Q., and Dang, Y., 2015, Re–Os isochron ages for arsenopyrite from Carlin–like gold deposits in the Yunnan–Guizhou–Guangxi "golden triangle", southwestern China. Ore Geology Reviews, v. 64, pp. 316–327.

Cheng, Y.S., and Cheng, P., 2014, Ore–forming material of Dachang tin deposit in Guangxi, China: lead isotope evidence. Trans Nonferrous Metals Society of China, v. 24, pp. 3652–3659. doi:10.1016/S1003–6326(14)63511–1.

Christensen, J.N., Halliday, A.N., Leigh, K.E., Randell, R.N., and Kesler, S.E., 1995, Direct dating of sulfides by Rb–Sr: a critical test using the Polaris Mississippi Valley-type Zn–Pb deposit. Geochimica Et Cosmochimica Acta, v. 59, pp. 5191–5197. doi:10.1016/0016–7037(95)00345–2.

Claypool, G.E., Holser, W.T., Kaplan, I.R., Sakai, H., and Zak, I., 1980, The age curves of sulfur and oxygen isotopes in marine sulfate and their mutual interpretation. Chemical Geology, v. 28, pp. 199–260. doi:10.1016/0009–2541(80)90047–9.

Coplen, T.B., Kendall, C., and Hopple, J., 1983, Comparison of stable isotope reference samples. Nature, v. 302, pp. 236–238. doi:10.1038/302236a0.

Friedman, I., and O'Neil, J.R., 1977, Compilation of Stable Isotope Fractionation Factors of Geochemical Interest. Data of Geochemistry, U.S:

Geological Survey Professional Paper, v. 440–KK, pp. 1–12.

Gao, J., Yang, R., Tao, P., Cheng, W., and Wei, H., 2013, Discovery of an abnormally high–$\delta^{34}S$ barite deposit and a new understanding of global sulfur isotope variation during geological history. Chinese Journal of Geochemistry, v. 32, pp. 321–325. doi:10.1007/s11631–013–0638–y.

Gupta, C.K., and Krishnamurthy, N., 2005, Extractive Metallurgy of Rare Earths CRC Press. Boca Raton, Florida, v. 65, pp.70–75.

Han, R.S., Chen, J., Li, Y., Gao, D.R., and Ma, D.Y., 2001, Discovery of concealed No.8 orebody at Qilinchang lead–zinc deposit in Huize mine, Yunnan. Geology–Geochemistry, v. 29, pp. 191–195 (in Chinese with English abstract).

Han, R.S., Liu, C.Q., Huang, Z.L., Ma, D.Y., Li, Y., Hu, B., Ma, G.S., and Lei, L., 2004, Fluid inclusion of calcite and sources of ore-forming fluids in the Huize Zn–Pb–(Ag–Ge) district, Yunnan, China. Acta Geologica Sinica (English Edition), v. 78, pp. 583–591.

Han, R.S., Chen, J., Huang, Z.L., Ma, D.Y., Xue, C.D., Li, Y., Zou, H.J., Li, B., and Hu, Y.Z., 2006, Dynamics of tectonic ore–forming process and localization prognosis of concealed ore– bodies– as exemplified by the Huize super–large Zn–Pb–(Ag–Ge) District, Yunnan. China Science Press, Beijing, v. 1, pp. 128–158 (in Chinese with English abstract).

Han, R.S., Liu, C.Q., Huang, Z.L., Chen, J., Ma, D.Y., Lei, L., and Ma, G.S., 2007, Geological features and origin of the Huize carbonate–hosted Zn–Pb–(Ag) District, Yunnan, South China. Ore Geology Reviews, v. 31, pp. 360–383. doi:10.1016/j.oregeorev.2006.03.003.

Han, R.S., Hu, Y.Z., Wang, X.K., Hou, B.H., Huang, Z.L., Chen, J., Wang, F., Wu, P., Li, B., Wang, H.J., Dong, Y., and Lei, L., 2012, Mineralization model of rich Ge–Ag–bearing Zn–Pb polymetallic deposit concentrated district in northeastern Yunnan. China. Acta Geologica Sinica, v. 86, pp. 280–294 (in Chinese with English abstract).

Han, R.S, Li, W., Qiu, W., Ren, T., and Wang, F., 2014, Typical Geological Features of Rich Zn-Pb-(Ge-Ag) Deposits in Northeastern Yunnan, China. Acta Geologica Sinica-English Edition, v. 88, pp. 160–162. doi:10.1111/1755–6724.12369_9.

Han, R., Li, B., Ni, P., Qiu, W., Wang, X., and Wang, T., 2016, Infrared micro–thermometry of fluid inclusions in sphalerite and geological significance of Huize super–large Zn–Pb–(Ge–Ag) deposit, Yunnan province. Journal of Jilin University (Earth Science Edition), v. 46, pp. 91–104.

Heijlen, W., Muchez, P., Banks, D.A., Schneider, J., Kucha, H., and Keppens, E., 2003, Carbonate–hosted Zn–Pb deposits in Upper Silesian, Poland: origin and evolution of mineralizing fluids and constraints on genetic models. Economic Geology, v. 98, pp. 911–932.

Hoefs, J., 1987, Stable isotope geochemistry, third edition. Springer–Verlag, Berlin Heidelberg, v. 9, 241 p. doi:10.1007/978–3–662–09998–8.

Hoefs, J., 2009, Stable isotope geochemistry, sixth edition. Springer–Verlag, Berlin Heidelberg, v. 12, 286 p. doi:10.1007/978–3–540–70708–0.

Hu, R.Z., and Zhou, M.F., 2012, Multiple Mesozoic mineralization events in South China –an introduction to the thematic issue. Mineralium Deposita, v. 47, pp. 579–588.

Hu, R.Z., Fu, S., Huang, Y., Zhou, M., Fu, S., Zhao, C., Wang, Y., Bi, X., and Xiao, J., 2017, The giant South China Mesozoic low–temperature metallogenic domain: reviews and a new geodynamic model. Journal of Asian Earth Sciences, v. 137, pp. 9–34.

Huang, Z.L., Li, W.B., Chen, J., Han, R.S., Liu, C.Q., Xu, C., and Guan, T., 2003, Carbon and oxygen isotope constraints on mantle fluid involvement in the mineralization of the Huize super-large Pb-Zn deposits, Yunnan Province, China. Journal of Geochemical Exploration, v. 78, pp. 637–642.

Jin, Z.G., Zhou, J.X., Huang, Z.L., Ye, L., Luo, K., Gao, J.G., Chen, X.L., Wang, B., and Peng, S., 2016, Ore genesis of the Nayongzhi Pb–Zn deposit, Puding city, Guizhou Province, China: evidences from S and in situ Pb isotopes. Acta Petrologica Sinica, v. 32, pp. 3441–3455 (in Chinese with English abstract).

Leach, D.L., Sangster, D., Kelley, K.D., Large, R.R., Garven, G., Allen, C., Gutzmer, J., and Walters, S., 2005, Sediment–hosted lead–zinc deposits: a global perspective. Economic Geology 100th Anniversary, pp. 561–607.

Leach, D.L., Bradley, D.C., Huston, D., Pisarevsky, S.A., Taylor, R.D., and Gardoll, S.J., 2010, Sediment–hosted lead–zinc deposits in Earth history. Economic Geology, v. 105, pp. 593–625. doi:10.2113/gsecongeo.105.3.593.

Li, W.B., Huang, Z.L., Wang, Y.X., Chen, J., Han, R.S., Xu, C., and Yin, M.D., 2004, Age of the giant Huize Zn–Pb deposits determined by Sm–Nd dating of hydrothermal calcite. Geological Review, v. 50, pp. 189–195.

Li, Q.L., Chen, F.K., Wang, X.L., and Li, C.F., 2005, Ultra–low procedural blank and the single grain mica Rb–Sr isochron dating. China Science Bulletin, v. 50, pp. 2861–2865. doi:10.1360/982005–984.

Li, X.B., Huang, Z.L., Li, W.B., Zhang, Z.L., and Yan, Z.F., 2006, Sulfur isotopic compositions of the Huize super–large Pb–Zn deposit, Yunnan Province, China: implications for the source of sulfur in the ore–forming fluids. Journal of Geochemical Exploration, v. 89, pp. 227–230. doi:10.1016/j.gexplo.2005.12.017.

Li, W.B., Huang, Z.L., and Yin, M.D., 2007, Dating of the giant Huize Zn–Pb ore field of Yunnan province, southwest China: constraints from the Sm–Nd system in hydrothermal calcite. Resource Geology, v. 57, pp. 90–97. doi:10.1111/j.1751–3928.2006.00007.x.

Li, H.T., Cao, D.Y., Wang, L.J., Guo, A.J., Li, Y.F., and Xu, H., 2013, Characteristics and evolution of coal–controlled structures on the east slope of the Xuefengshan domain in central Hunan Province. Geotectonica et Metallogenia, v. 37, pp. 611–621 (in Chinese with English abstract).

Li, B., Zhou, J.X., Huang, Z.L., Yan, Z.F., Bao, G.P., and Sun, H.R., 2015, Geological, rare earth elemental and isotopic constraints on the origin of the Banbanqiao Zn–Pb deposit, southwest China. Journal of Asian Earth Sciences, v. 111, pp. 100–112.

Lin, Z.Y., Wang, D.H., and Zhang, C.Q., 2010, Rb–Sr isotopic age of sphalerite from the Paoma lead–zinc deposit in Sichuan Province and its implications. Geological China, v. 37, pp. 488–494 (in Chinese with English abstract).

Liu, H.C., and Lin, W.D., 1999, Study on the Law of Pb–Zn–Ag Ore Deposit in Northeast Yunnan, China. Yunnan University Press, Kunming, pp. 1–468 (in Chinese).

Liu, J.M., and Liu, J.J., 1997, Basin fluid genetic model of sediment–hosted micro–disseminated gold deposits in the gold–triangle area between Guizhou, Guangxi and Yunnan. Acta Mineralogica Sinica, v. 17, pp. 448–456 (in Chinese with English abstract).

Mao, J.W., Zhou, Z.H., Feng, C.Y., Wang, Y.T., Zhang, C.Q., Peng, H.J., and Yu, M., 2012, A preliminary study of the Triassic large–scale mineralization in China and its geodynamic setting. Geological China, v. 39, pp. 1437–1471 (in Chinese with English abstract).

Meng, Y.M., Hu, R.Z., Huang, X.W., Gao, J.F., and Sasseville, C., 2019, The origin of the carbonate-hosted Huize Zn-Pb-Ag deposit, Yunnan province, SW China: constraints from the trace element and sulfur isotopic compositions of pyrite. Mineralogy and Petrology, v. 113, pp. 369–391.

Muchez, P., Heijlen, W., Banks, D., Blundell, D., Boni, M., and Grandia, F., 2005, Extensional tectonics and the timing and formation of basin–hosted deposits in Europe. Ore Geology Reviews, v. 27, pp. 241–267. doi:10.1016/j.oregeorev.2005.07.013.

Nakai, S., Halliday, A.N., Kesler, S.E., Jones, H.D., Kyle, J.R., and Lanes, T.E., 1993, Rb–Sr dating of sphalerite from Mississippi Valley–type (MVT) ore deposits. Geochimica Et Cosmochimica Acta, v. 57, pp. 417–427. doi:10.1016/0016–7037(93)90440–8.

Ohmoto, H., 1972, Systematics of sulfur and carbon isotopes in hydrothermal ore deposits. Economic Geology, v. 67, pp. 551–579. doi:10.2113/gsecongeo.67.5.551.

Ohmoto, H., and Rye, R.O., 1979, Isotopes of sulfur and carbon, in Barnes, H.L., ed., Geochemistry of hydrothermal ore deposits, (second edition). New York, Wiley, pp. 509–567.

Ohmoto, H., and Goldhaber, M.B., 1997, Sulfur and carbon isotopes, in

Barnes, H.L., ed., Geochemistry of hydrothermal ore deposits, (third edition). New York, Wiley, pp. 517–611.

Pass, H.E., Cooke, D.R., Davidson, G., Maas, R., Dipple, G., Rees, C., Ferreira, L., Taylor, C., and Deyell, C.L., 2014, Isotope geochemistry of the northeast zone, Mount Polley alkalic Cu–Au–Ag porphyry deposit, British Columbia: a case for carbonate assimilation. Economic Geology, v. 109, pp. 859–890. doi:10.2113/econgeo.109.4.859.

Platt, A.W.G., 2012, Group trends, in Atwood, D.A., ed., The rare earth elements-fundamentals and applications. Wiley, Chichester, pp. 44–53.

Qi, L., Hu, J., and Gregoire, D.C., 2000, Determination of trace elements in granites by inductively coupled plasma mass spectrometry. Talanta, v. 51, pp. 507–513.

Rddad, L., Mouguina, E.M., Muchez, P., and Darling, R.S., 2018, The genesis of the Ali Ou Daoud Jurassic carbonate Zn–Pb Mississippi Valley–type deposit, Moroccan central High Atlas: Constraints from bulk stable C–O–S, in situ radiogenic Pb isotopes, and fluid inclusion studies. Ore Geology Reviews, v. 99, pp. 365–379. doi:10.1016/j.oregeorev.2018.06.020.

Reid, A., Wilson, C.J.L., Shun, L., Pearson, N., and Belousova, E., 2007, Mesozoic plutons of the Yidun Arc, SW China: U–Pb geochronology and Hf isotopic signature. Ore Geology Reviews, v. 31, pp. 88–106. doi:10.1016/j.oregeorev.2004.11.003.

Rye, R.O., and Ohmoto, H., 1974, Sulfur and carbon isotopes and ore genesis: a review. Economic Geology, v. 69, pp. 826–842. doi:10.2113/gsecongeo.69.6.826.

Seal, I.R., 2006, Sulfur isotope geochemistry of sulfide minerals. Review of Mineralogy and Geochemistry, v. 61, pp. 633–677. doi:10.2138/rmg.2006.61.12.

Shen, S., 1988, The metallogenic rule ore–search orientation of the major ore resources at the Xichang–Middle Yunnan area. Chongqing Publishing House, Chongqing, pp. 78–123 (in Chinese with English abstract).

Sun, W.H., Zhou, M.F., Gao, J.F., Yang, Y.H., Zhao, X.F., and Zhao, J.H., 2009, Detrital zircon U–Pb geochronological and Lu–Hf isotopic constraints on the Precambrian magmatic and crustal evolution of the western Yangtze Block, SW China. Precambrian Research, v. 172, pp. 99–126. doi:10.1016/j.precamres.2009.03.010.

Taylor, J.H.P., Frechen, J., and Degens, E.T., 1967, Oxygen and carbon isotope studies of carbonatites from the Laacher See District, West Germany and the Alno District Sweden. Geochimica Et Cosmochimica Acta, v. 31, pp. 407–430. doi:10.1016/0016–7037(67)90051–8.

Thode, H.G., 1970, Sulfur isotope geochemistry and fractionation between coexisting sulfide minerals. Journal of the Mineralogical Society of America, Special Paper, v. 3, pp. 133–144.

Tu, G.Z., 1984, Geochemistry of Strata–bound Ore Deposits in China. Science Press, Beijing, v. 1, pp. 13–69 (in Chinese with English abstract).

Veizer, J., and Hoefs, J., 1976, The nature of O^{18}/O^{16} and C^{13}/C^{12} secular trends in sedimentary carbonate rocks. Geochimica Et Cosmochimica Acta, v. 40, pp. 1387–1395.

Wang, X.C., Zheng, Z.R., Zheng, M.H., and Xu, X.H., 2000, Metallogenic mechanism of the Tianbaoshan Pb–Zn deposit, Sichuan. Chinese Journal of Geochemistry, v. 19, pp. 121–133.

Xie, J.R., 1963, Introduction of the Chinese Ore Deposits. Scientific Books Publishing House, Beijing, pp. 1–71 (in Chinese).

Yan, D.P., Zhou, M.F., Song, H.L., Wang, X.W., and Malpas, J., 2003, Origin and tectonic significance of a Mesozoic multi–layer over–thrust system within the Yangtze Block (South China). Tectonophysics, v. 361, pp. 239–254. doi:10.1016/S0040–1951(02)00646–7.

Yan, Z.F., Huang, Z.L., Xu, C., Chen, M., and Zhang, Z.L., 2007, Signatures of the source for the Emeishan flood basalts in the Ertan area: Pb isotope evidence. Chinese Journal of Geochemistry, v. 26, pp. 207–213.

Yin, M.D., Huang, Z.L., and Li, W.B., 2009, Rb–Sr isotopic dating of sphalerite from the giant Huize Pb–Zn ore field, Yunnan province, southwestern China. Chinese Journal of Geochemistry, v. 28, pp. 70–75. doi:10.1007/s11631–009–0070–5.

Zartman, R.E., and Doe, B.R., 1981, Plumbotectonics–the model. Tectonophysics, v. 75, pp.135–162.

Zaw, K., Peters, S.G., Cromie, P., Burrett, C., and Hou, Z., 2007, Nature, diversity of deposit types and metallogenic relations of South China. Ore Geology Reviews, v. 31, pp. 3–47. doi:10.1016/j.oregeorev.2005.10.006.

Zhang, W.J., 1984, A preliminary discussion on the sedimentary origin and metallogenic rule of Pb–Zn deposits in northeastern Yunnan. Journal of Geology and Exploration, v. 7, pp. 11–16 (in Chinese with English abstract).

Zhang, Y.X., and Yuan, X.C., 1988, Panxi Rift. Geological Publishing House, Beijing, pp. 5–63 (in Chinese with English abstract).

Zhang, X.C., 1989, Geological characteristics and chemical composition of deep ores in the No. 1 orebody of the Kuangshanchang Pb–Zn deposit. A research report, pp. 6–54 (in Chinese).

Zhang, Z.L., Huang, Z.L., Rao, B., Guan, T., and Yan, Z.F., 2005a, Concentration mechanism of ore–forming fluid in Huize lead–zinc deposits, Yunnan Province. Earth Science, v. 30, pp. 443–450.

Zhang, Z.L., Huang, Z.L., Rao, B., Li, W.B., and Yan, Z.F., 2005b, Study on the ore–forming fluid characteristics of Huize Pb–Zn ore deposits. Contributions to Geology and Mineral Resources Research, v. 20, pp. 115–122 (in Chinese with English abstract).

Zhang, Z.B., Li, C.Y., Tu, G.C., Xia, B., and Wei, Z.Q., 2006, Geotectonic evolution background and ore–forming process of Pb–Zn deposits in Chuan–Dian–Qian area of southwest China. Geotectonica et Metallogenia, v. 30, pp. 343–354.

Zhang, C.Q., 2008, The genetic model of Mississippi Valley–type deposits in the boundary area of Sichuan, Yunnan and Guizhou Province, China. Doctor Dissertation, China University of Geosciences, Beijing. pp. 1–39 (in Chinese with English abstract).

Zhang, C.Q., Wu, Y., Hou, L., and Mao, J.W., 2015, Geodynamic setting of mineralization of Mississippi Valley–type deposits in world–class Sichuan–Yunnan–Guizhou Zn–Pb triangle, southwest China: implications from age–dating studies in the past decade and the Sm–Nd age of the Jinshachang deposit. Journal of Asian Earth Science, v. 103, pp. 103–114.

Zhang, Y., Han, R., Wei, P., and Wang, L., 2017, Identification of Two Types of Metallogenic Fluids in the Ultra–Large Huize Pb–Zn Deposit, SW China. Geofluids, pp. 1–22.

Zhao, Z., 1995, Metallogenic model of Pb–Zn deposits in northeastern Yunnan. Journal of Yunnan Geology, v. 14, pp. 350–354 (in Chinese with English abstract).

Zheng, M.H., and Wang, X.C., 1991, Genesis of the Daliangzi Pb–Zn deposit in Sichuan, China. Economic Geology, v. 86, pp. 831–846.

Zheng, Y.F., and Chen, J.F., 2000, Stable Isotope Geochemistry. Science Press, Beijing, pp. 10–50 (in Chinese).

Zhong, K.H., Liao, W., Song, M.Y., and Zhang, Y.Q., 2013, Discussion on sulfur isotope of Huize Pb–Zn deposit in Yunnan, China. Journal of Chengdu University of Technology (Science and Technology Edition), v. 40, pp. 130–138.

Zhong, Y.T., He, B., Mundil, R., and Xu, Y.G., 2014, CA–TIMS zircon U–Pb dating of felsic ignimbrite from the Binchuan section: implications for the termination age of Emeishan large igneous province. Lithos, v. 204, pp. 14–19. doi:10.1016/j.lithos.2014.03.005.

Zhou, C.X., Wei, C.S., and Guo, J.Y., 2001, The source of metals in the Qilingchang Pb–Zn deposit, Northeastern Yunnan, China: Pb–Sr isotope constraints. Economic Geology, v. 96, pp. 583–598. doi:10.2113/gsecongeo.96.3.583.

Zhou, M.F., Malpas, J., Song, X.Y., Kennedy, A.K., Robinson, P.T., Sun, M., Lesher, M., and Keays, R.R., 2002a, A temporal link between the Emeishan large igneous province (SW China) and the end–Guadalupian mass extinction. Earth Planetary Science Letters, v. 196, pp. 113–122. doi:10.1016/S0012–821X(01)00608–2.

Zhou, J.X., Huang, Z.L., Zhou, M.F., Li, X.B., and Jin, Z.G., 2013a, Constraints of C–O–S–Pb isotope compositions and Rb–Sr isotopic age on the origin of the Tianqiao carbonate–hosted Pb–Zn deposit, SW China.

Ore Geology Reviews, v. 53, pp. 77–92.
Zhou, J.X., Huang, Z.L., and Bao, G.P., 2013b, Geological and sulfur–lead–strontium isotopic studies of the Shaojiwan Pb–Zn deposit, southwest China: implications for the origin of hydrothermal fluids. Journal of Geochemical Exploration, v. 128, pp. 51–61.
Zhou, J.X., Gao, J.G., Chen, D., Liu, and X.K., 2013c, Ore genesis of the Tianbaoshan carbonate–hosted Pb–Zn deposit, Southwest China: geologic and isotopic (C–H–O–S–Pb) evidence. International Geology Review, v. 55, pp. 1300–1310.
Zhou, J.X., Huang, Z.L., and Yan, Z.F., 2013d, The origin of the Maozu carbonate–hosted Pb–Zn deposit, southwest China: constrained by C–O–S–Pb isotopic compositions and Sm–Nd isotopic age. Journal of Asian Earth Sciences, v. 73, pp. 39–47.
Zhou, J.X., Huang, Z.L., Gao, J.G., and Yan, Z.F., 2013e, Geological and C–O–S–Pb–Sr isotopic constraints on the origin of the Qingshan carbonate–hosted Pb–Zn deposit, SW China. International Geology Review, v. 55, pp. 904–916. doi:10.1080/00206814.2013.767496.
Zhou, J.X., Huang, Z.L., Lv, Z.C., Zhu, X.K., Gao, J.G., and Mirnejad, H., 2014, Geology, isotope geochemistry and ore genesis of the Shanshulin carbonate–hosted Pb–Zn deposit, southwest China. Ore Geology Reviews, v. 63, pp. 209–225. doi:10.1016/j.oregeorev.2014.05.012.
Zhou, J.X., Bai, J.H., Huang, Z.L., Zhu, D., Yan, Z.F., and Lv, Z.C., 2015, Geology, isotope geochemistry and geochronology of the Jinshachang carbonate–hosted Pb–Zn deposit, South China. Journal of Asian Earth Sciences, v. 98, pp. 272–284.
Zhou, J.X., Luo, K., Wang, X.C., Wilde, S.A., Wu, T., Huang, Z.L., Cui, Y.L., and Zhao, J.X., 2018, Ore genesis of the Fule Pb–Zn deposit and its relationship with the Emeishan Large Igneous Province: Evidence from mineralogy, bulk C–O–S and in situ S–Pb isotopes. Gondwana Research, v. 54, pp. 161–179. doi:10.1016/j.gr.2017.11.004.

Abiola Oyebamiji is a PhD student at the Institute of Geochemistry, University of Chinese Academy of Sciences. His research activity is focused on the continental geodynamics and metallogeny of low-temperature mineralization with special attention to the origin of MVT lead-zinc deposits in the Southwestern part of China. His exceptional and distinctive abilities made him a beneficiary of the 2016 CAS-TWAS President's Fellowship.

Aizat Zhaanbaeva is a PhD candidate at the Institute of Geochemistry, University of Chinese Academy of Sciences. Her research focus on geology and geochemistry of Carlin-type gold deposits.

Ruizhong Hu is the Director of the State Key Laboratory of Ore Deposit Geochemistry, Institute of Geochemistry, Chinese Academy of Sciences, Guiyang, China. His research interests are focused on continental geodynamics and metallogeny, ore deposit geochemistry, metallogenic regularity and prognosis and geochemistry of noble gas isotopes.

Tehseen Zafar is a PhD research scholar at the Institute of Geochemistry, University of Chinese Academy of Sciences. He is awardee of CAS-TWAS Scholarship. His research focus on petrogenetic studies and geochemical evaluation of mafic-ultramafic complex.

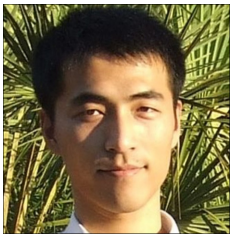

Chenghai Zhao is a Post Doctor and Geologist at Institute of Geochemistry, Chinese Academy of Sciences. He has worked as an Exploration Geologist at several gold mining companies. He has published several papers on Carlin-type gold and epithermal deposits in China.

Table SI. REE concentrations (ppm) of Calcite and sulfide extracts

Sample no	Mineral	La	Ce	Pr	Nd	Sm	Eu	Gd	Tb	Dy	Ho	Er	Tm	Yb	Lu	∑REE	δEu	LaN/YbN
HZ1	Calcite	2.723	5.304	0.843	3.629	0.853	0.153	0.824	0.137	0.838	0.164	0.442	0.062	0.372	0.056	16.40	0.56	4.93
HZ2	Calcite	2.983	5.462	0.865	3.797	0.870	0.159	0.856	0.141	0.857	0.168	0.452	0.064	0.381	0.056	17.11	0.56	5.28
HZ5	Calcite	1.300	2.235	0.225	0.924	0.184	0.039	0.178	0.029	0.181	0.037	0.109	0.016	0.095	0.015	5.57	0.66	9.20
HZ6	Calcite	1.280	2.183	0.227	0.896	0.175	0.037	0.170	0.027	0.167	0.035	0.104	0.015	0.096	0.015	5.43	0.66	8.96
HZ7	Calcite	1.982	2.984	0.356	1.425	0.268	0.051	0.239	0.039	0.251	0.054	0.161	0.025	0.156	0.024	8.01	0.62	8.58
HZ8	Calcite	2.056	3.019	0.358	1.443	0.268	0.052	0.244	0.040	0.250	0.054	0.158	0.025	0.154	0.024	8.14	0.62	9.01
HZ9	Calcite	2.057	3.024	0.350	1.413	0.267	0.051	0.240	0.039	0.248	0.053	0.159	0.024	0.157	0.024	8.11	0.61	8.86
HZ10	Calcite	4.386	11.590	1.310	5.465	1.185	0.206	1.006	0.158	0.923	0.181	0.513	0.075	0.454	0.067	27.52	0.58	6.51
HZ12	Calcite	1.468	4.769	0.643	2.944	0.713	0.125	0.555	0.095	0.582	0.113	0.330	0.052	0.326	0.047	12.76	0.61	3.03
HZ20	Calcite	1.739	3.739	0.488	2.061	0.466	0.104	0.445	0.071	0.444	0.094	0.267	0.039	0.231	0.035	10.22	0.70	5.07
HZ23	Calcite	3.230	5.430	0.745	2.792	0.556	0.107	0.475	0.072	0.408	0.078	0.219	0.031	0.191	0.028	14.36	0.64	11.39
HZ24	Calcite	2.288	3.332	0.418	1.572	0.305	0.056	0.281	0.044	0.268	0.056	0.165	0.025	0.153	0.023	8.98	0.58	10.10
HZQ-7-11a	Pyrite	0.0613	0.1443	0.0163	0.0925	0.0394	0.0067	0.0333	0.0054	0.0344	0.0073	0.0203	0.0035	0.0229	0.0037	0.49	0.57	1.80
HZQ-3-10	Pyrite	0.1705	0.2365	0.0181	0.0627	0.0132	0.0046	0.0115	0.0019	0.0138	0.0031	0.0097	0.0015	0.0117	0.0020	0.56	1.14	9.83
HZQ-3b	Pyrite	0.1175	0.3150	0.0296	0.1191	0.0238	0.0176	0.0265	0.0062	0.0575	0.0156	0.0585	0.0100	0.0664	0.0097	0.87	2.14	1.19
HZQ-11g	Pyrite	0.0884	0.2267	0.0270	0.1457	0.0636	0.0202	0.0558	0.0093	0.0661	0.0152	0.0509	0.0096	0.0658	0.0105	0.85	1.04	0.91
HZQ-11c-1	Pyrite	0.0564	0.1176	0.0129	0.0691	0.0393	0.0072	0.0466	0.0087	0.0637	0.0140	0.0453	0.0082	0.0566	0.0097	0.56	0.51	0.67
HZQ-3-9	Pyrite	0.0718	0.1563	0.0164	0.0680	0.0188	0.0046	0.0139	0.0023	0.0144	0.0030	0.0097	0.0017	0.0101	0.0014	0.39	0.86	4.78
HZQ-13-7	Galena	0.0099	0.0237	0.0021	0.0104	0.0038	0.0009	0.0046	0.0009	0.0064	0.0014	0.0037	0.0006	0.0043	0.0007	0.07	0.62	1.55
HZQ-7-9a	Galena	0.0059	0.0058	0.0002	0.0012	0.0445	0.0000	0.0000	0.0002	0.0005	0.0000	0.0000	0.0000	0.0004	0.0000	0.06	0.05	10.16
HZQ-13-10	Galena	0.0024	0.0059	0.0004	0.0020	0.0023	0.0001	0.0007	0.0001	0.0007	0.0001	0.0004	0.0001	0.0005	0.0000	0.02	0.36	3.24
HZQ-13a	Galena	0.0369	0.0755	0.0066	0.0291	0.0089	0.0016	0.0111	0.0024	0.0166	0.0037	0.0108	0.0016	0.0104	0.0014	0.22	0.50	2.40
HZQ-13-1-3	Sphalerite	0.0478	0.1482	0.0143	0.0622	0.0146	0.0027	0.0145	0.0023	0.0148	0.0032	0.0103	0.0019	0.0124	0.0019	0.35	0.56	2.60
HZQ-3-4	Sphalerite	0.0022	0.0047	0.0004	0.0019	0.0023	0.0002	0.0008	0.0001	0.0009	0.0002	0.0006	0.0001	0.0006	0.0001	0.02	0.38	2.55
HZQ-11e	Sphalerite	0.1100	0.3329	0.0392	0.1993	0.0644	0.0161	0.0619	0.0097	0.0564	0.0108	0.0292	0.0044	0.0283	0.0040	0.97	0.78	2.62
HZQ-7-7	Sphalerite	0.0517	0.1187	0.0110	0.0496	0.0104	0.0052	0.0094	0.0011	0.0071	0.0015	0.0042	0.0007	0.0042	0.0007	0.28	1.60	8.38
HZQ-4	Sphalerite	0.1190	0.3041	0.0307	0.1327	0.0308	0.0074	0.0265	0.0043	0.0245	0.0049	0.0128	0.0018	0.0111	0.0016	0.71	0.79	7.21
HZQ-14-2b	Sphalerite	0.0301	0.1222	0.0166	0.0965	0.0326	0.0066	0.0302	0.0038	0.0193	0.0030	0.0061	0.0007	0.0032	0.0004	0.37	0.65	6.32
HZQ-14-6	Sphalerite	0.1228	0.2648	0.0206	0.0756	0.0157	0.0062	0.0164	0.0032	0.0258	0.0070	0.0260	0.0051	0.0388	0.0061	0.63	1.19	2.13
HZQ-13-5	Sphalerite	0.1421	0.4525	0.0454	0.1722	0.0333	0.0044	0.0293	0.0052	0.0359	0.0081	0.0272	0.0047	0.0338	0.0050	1.00	0.43	2.83

$\delta Eu = Eu/Eu^* = Eu_N/[(Sm_N + Gd_N) \times 0.5]$.